International Journal of Coal Geology 268 (2023) 104198

Contents lists available at ScienceDirect

International Journal of Coal Geology

journal homepage: www.elsevier.com/locate/coal

Geochemistry and organic petrography of the Middle Permian Lucaogou alkaline lacustrine oil shale in the southern Junggar Basin, China: Implications for formation conditions and organic matter accumulation

Jinqi Qiao [a,b], Qingyong Luo [a,b,*], Kuihua Zhang [c], Guanlong Zhang [c], Jincai Duan [a,b], Dandan Wang [a,b], Hongzhou Yu [c], Shengzhu Wang [c], Yansheng Qu [c], Ludmila Kopaevich [d]

[a] State Key Laboratory of Petroleum Resources and Prospecting, China University of Petroleum, Beijing 102249, China
[b] Basin and Reservoir Research Center, China University of Petroleum, Beijing 102249, China
[c] Exploration and Development Research Institute of Shengli Oilfield, SINOPEC, Dongying, Shandong 257061, China
[d] Lomonosov Moscow State University, GSP-1, Leninskie Gory, Moscow 119991, Russia

ARTICLE INFO

Keywords:
Elements
Organic petrography
Alkaline lacustrine oil shale
Lucaogou Formation
Junggar Basin
Depositional environment
Paleoclimate

ABSTRACT

Organic matter (OM) accumulation in terrestrial sediments shows not only a significant carbon sink in the Earth's carbon cycle but an important origin of fossil fuels, which is closely associated with the complex and diverse depositional environments and climate conditions. The Junggar Basin developed the most laterally extensive and thickest alkaline lacustrine sediments as well as the richest hydrocarbon source rock/oil shale interval of all the world during the deposition of the Lucaogou Formation and equivalent units. In this study, the sedimentary succession of 564 m with a mudstone and dolomite matrix of the Lucaogou oil shale from the Qi 1 well located in the southern Junggar Basin was investigated, which can be divided into two members based on lithology. This paper is a synthetic use of major element oxides, trace, and rare-earth elements as well as organic petrography data as proxies to evaluate the provenance, paleotectonic setting, paleoclimate and weathering conditions, paleoenvironment, and paleoproductivity as well as origin and accumulation of OM of the Lucaogou sediments.

It is suggested that no recycling sediments in all the studied samples, based on parameters including the Th/Sc vs. Zr/Sc plot, the Chemical Index of Alteration (CIA) being linearly dependent on Weathering Index of Parker (WIP), and the high Index of Compositional Variability. The provenance mainly from intermediate-felsic volcanic rocks (e.g., granodiorite, andesite and dacite) is supported by the bivariate plots of Eu_{anom} vs. Th/Sc, La/Th vs. Hf, La/Sc vs. Co/Th, Cr/Th vs. Sc/Th, Y/Ni vs. Cr/V, and Nb/Y vs. Zr/TiO_2 as well as triangular diagrams of mafic–felsic–weathering, M^+–4Si–R^{2+} and Rb/V–Zr/Zn–Sc/Nb. The continental island arc is inferred from paleotectonic setting discrimination diagrams (i.e., the La–Th–Sc, Th–Co–Zr/10 and Th–Sc–Zr/10 ternary as well as Ti/Zr vs. La/Sc binary diagrams). The chemical weathering indices (i.e., the CIA, WIP, weathering index (W), Weathering Intensity Scale, Sodium Depletion Index, and Ga/Rb vs. K_2O/Al_2O_3 binary diagram) indicate the paleoclimate conditions were cold/arid with weak chemical weathering in a warming and/or enhanced continental weathering episode. Besides, the Sr/Ba ratios and gallium concentrations indicate the paleosalinity was brackish to hypersaline and was higher in the lower member in relation to that in the upper member. However, the suboxic environment of the benthic water (inferred from the Mo_{EF} vs. U_{EF} co-variations and C_{org}/P ratios as well as large sizes of framboidal pyrites) and the moderate paleoproductivity (evaluated via the Si_{bio}, Ba_{bio}, and P_{bio} values, as well as Ni/Al and Cu/Al ratios) caused by predominate algae and bacteria (inferred from the organic petrography) kept stable in the paleolake during this period. The OM accumulation was mainly controlled by the preservation conditions rather than the paleoproductivity and limited detrital inputs/low deposition rates, which was indicated by the plot of Co × Mn values vs. Cd/Mo ratios and the total organic carbon contents being negatively related to stable carbon isotope compositions of OM.

* Corresponding author at: Basin and Reservoir Research Center, China University of Petroleum, No. 18, Fuxue Road, Changping District, Beijing, China.
E-mail addresses: jinqi.qiao@cup.edu.cn (J. Qiao), qingyong.luo@cup.edu.cn (Q. Luo), quyansheng.slyt@sinopec.com (Y. Qu).

https://doi.org/10.1016/j.coal.2023.104198
Received 7 December 2022; Received in revised form 28 January 2023; Accepted 29 January 2023
Available online 2 February 2023

1. Introduction

Three of the five thickest and richest organic matter (OM) sediment intervals in the world developed in lake basins (Demaison and Huizinga, 1991). So, OM accumulation in terrestrial sediments is a significant carbon sink in the Earth's carbon cycle and is an important origin of fossil fuels (petroleum, microbial gas, coal, etc.), which is closely associated with conditions of climate and depositional environments (Carroll and Wartes, 2003; Dai et al., 2013; Huang et al., 2020; Qiao et al., 2021a). However, the formation conditions and OM accumulation mechanisms vary with the complex and diverse terrestrial depositional environments and regional climates. In the last decades, mudstone/shale, especially lacustrine mudstone/shale, has been paid more attention due to the rise of research related to shale-oil and shale-gas (Jarvie et al., 2007; Zou et al., 2010; Jarvie, 2012; Luo et al., 2016; Tian et al., 2016). Sedimentary rocks/sediments are the depositions of weathering products of provenance rocks transported via fluids, and their geochemical characteristics record this process and kinds of related information (Nesbitt and Young, 1982; Suttner and Dutta, 1986; Fedo et al., 1995; Dera et al., 2009; Ross and Bustin, 2009; Kemp et al., 2016; Song et al., 2018). Some major element oxides and a few trace elements in sedimentary rocks/sediments are climatically sensitive, so they can be used to interpret paleoclimate conditions (e.g., Parker, 1970; Nesbitt and Young, 1982; Fedo et al., 1995; Rasmussen et al., 2011; Meunier et al., 2013; Qiao et al., 2022). Meanwhile, several trace elements and rare-earth elements (REEs) are preserved well in sedimentary rocks/sediments because of their chemical immobility during the processes of weathering and diagenesis and thus are considered more reliable compared to major element oxides in interpreting paleotectonic settings and provenance materials (e.g., Floyd and Leveridge, 1987; McLennan et al., 1990; Mclennan, 1993; Cullers, 2002; Ryan and Williams, 2007; LaMaskin et al., 2008). Additionally, some redox- and salinity-sensitive trace elements can be used to reconstruct paleoredox (Jones and Manning, 1994; Tribovillard et al., 2006; Tribovillard et al., 2012) and paleosalinity (Salminen et al., 2005; Wei and Algeo, 2020) situations. Moreover, some major element oxides and trace elements can be used to evaluate paleoproductivity because their concentrations are mainly controlled by biological processes (Dymond et al., 1992; Tribovillard et al., 2006; Schoepfer et al., 2015; Shen et al., 2015; Arsairai et al., 2016). There are the following advantages to exploring the issues mentioned above by studying mudstone/shale. Firstly, over the whole geological history of the Earth, mudstone/shale makes up a large proportion of all rocks; secondly, mudstone/shale are more sensitive to climate change in comparison with tree rings as well as compositions of pollen and spores; thirdly, mudstone/shale records more information related to biological communities and hydrological conditions as compared with aeolian deposits; fourthly, compared with ice sheets, especially during interglacial stages, mudstone/shale is more widely distributed; finally, mudstones/shales are more representative of the geochemical information of provenance due to their impermeability and homogeneity of grain size in relation to coarse-grained sedimentary rocks/sediments which are more easily affected by hydraulic sorting effect (McCulloch and Wasserburg, 1978; Fischer et al., 1999; Bhat and Ghosh, 2001; Briffa et al., 2004; Potter et al., 2005; Svensson et al., 2006; Deng et al., 2011; Cai et al., 2012).

The Fengcheng Formation, deposited between the Late Carboniferous C4 (late Bashkirian–Moscovian) and Early Permian P1 (Asselian–early Sakmarian) glacial intervals during the Late Paleozoic Ice Age (LPIA), was regarded as the oldest alkaline lacustrine OM-rich shale in the region of the Junggar Basin (Fielding et al., 2008a, 2008b; Cao et al., 2020; Tang et al., 2021; Wang et al., 2022). Following the Fengcheng Formation, the world's richest and thickest alkaline lacustrine OM-rich interval (i.e., the Lucaogou Formation) was deposited in the Middle Permian Junggar Basin which was one of the largest known Phanerozoic lake basins and developed the most laterally extensive paleolake (i.e., a maximum area of approximately 300,000 km^2) (Demaison and Huizinga, 1991; Carroll, 1998; Wartes et al., 2002; Carroll and Wartes, 2003; Luo et al., 2018; Huang et al., 2020). The deposition of the Lucaogou Formation covered a period with an estimate of 3 Ma (Carroll and Wartes, 2003; Huang et al., 2020). It is unclear when the Lucaogou Formation began to deposit because the biostratigraphic features of the Lucaogou Formation have not yet been established systematically. For the sedimentary rocks/sediments, the maximum age of deposition that occurred can be determined by the youngest concordant detrital zircon age (Gehrels, 2014). The zircon U–Pb data from Yang et al. (2010) and Sun et al. (2022) indicates the Lucaogou Formation in the areas near the Bogda Mountains was deposited during the P1 glacial interval proposed by Fielding et al. (2008a, 2008b), i.e., between Sakamarian and Artinskian Stage, which contradicts the studies suggesting the Lucaogou Formation was deposited in Guadalupian Series (Wang et al., 2018; Huang et al., 2020; Zhao et al., 2020) corresponding to P3 and P4 glacial intervals in Siberia (Fielding et al., 2008a, 2008b). Despite the uncertainty of the absolute age and the fact that terrestrial sediments may be more sensitive to regional than to global-scale climate change, the study focusing on the Lucaogou Formation can provide important clues for the study of the formation mechanisms of the alkaline lacustrine oil shale and the regional paleoenvironment reconstruction in the study area.

In this contribution, a comprehensive study of geochemical data and organic petrology are utilized to interpret the provenance, paleotectonic setting, paleoclimate and weathering conditions, terrestrial input, paleoenvironment and paleoproductivity as well as origin and accumulation of OM of the Middle Permian oil shale.

2. Geologic setting

The Junggar Basin, a typical superimposed basin surrounded by tectonically active mountain ranges in present-day western China, is based on the combination of the Precambrian crystalline and part of the Hercynian folded basement (Qiao et al., 2020). The basin is triangular in shape, 370 km wide from south to north and 700 km from west to east, covering an area of approximately 130,000 km^2 (Cheng et al., 2022; Qiao et al., 2023). The evolution of the Junggar Basin experienced four tectonic evolution stages which are the Late Carboniferous-Early Permian marine and residual marine foreland basin, Middle-Late Permian continental foreland basin, Mesozoic intracontinental oscillatory depression basin, and Cenozoic regeneration foreland basin (Cao et al., 2005).

The Lucaogou Formation is a set of important OM-rich oil shale in the basin (Luo et al., 2018), which recorded a gradual shift from shallow to deep lake facies as well as low deposition rate and stable salinity stratification (Carroll, 1998). The Lucaogou Formation contradicts the traditional lacustrine source rock model in at least two important respects, i.e., the low to moderate primary productivities were controlled by limited nutrient supply dominated by intermediate volcanic rocks, and the formation occurred at middle paleolatitudes in contrast to the tropical latitudes (Fig. 1a and b; Carroll, 1998). Besides plenty of unconventional oil resources discovered in the Lucaogou shales from the southern Junggar Basin, the Lucaogou Formation is the main hydrocarbon source of the hydrocarbon reservoirs in the Permian Wutonggou Formation, Triassic Jiucaiyuan Formation and Jurassic Toutunhe Formation (Luo et al., 2018; Hou et al., 2021).

The studied Qi 1 well is located in the southern Junggar Basin and at the piedmont of the Bogda Mountains (Fig. 1c). The Bogda Mountains located in the southern Central Asian Orogenic Belt are part of the Chinese North Tianshan Orogenic Belt, which developed sedimentary and igneous rocks covering from Devonian to Quaternary (Fig. 1c; Allen et al., 1995). Previous studies argued that rocks of the Bogda Mountains sourced from the Central Tianshan Block and North Tianshan Orogenic Belt (e.g., Yang et al., 2013; Tang et al., 2014).

The thickness of the Lucaogou Formation is thinner as the distance from the Bogda Mountain foothills increases, which is approximately 1300 m in the Tianchi area (Carroll and Wartes, 2003), then decreases to

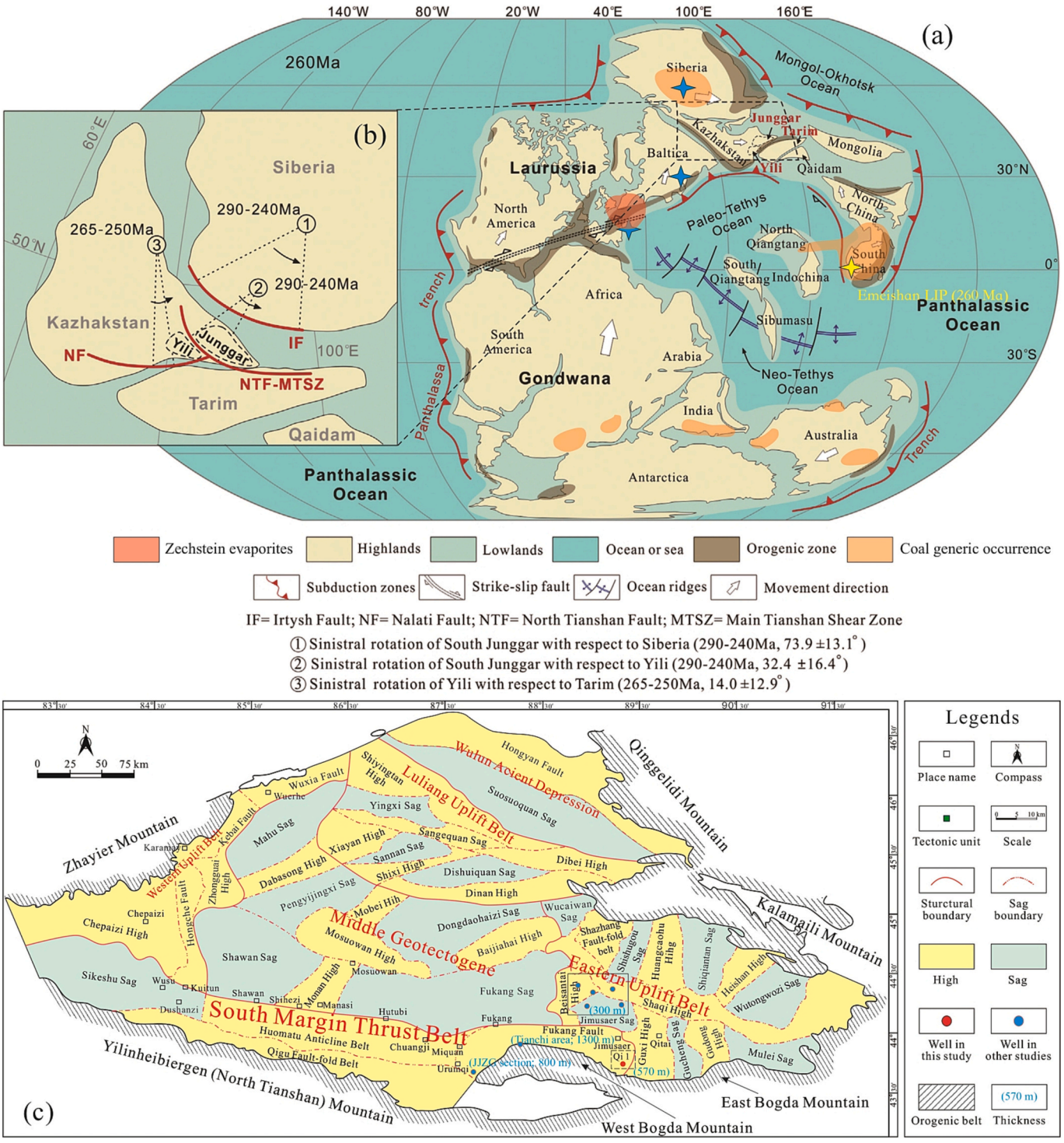

Fig. 1. (a and b) Schematic map showing the location of the Junggar Basin in the paleogeographic map at ca. 260 Ma (modified after Zhao et al., 2020) as well as (c) schematic map of the Junggar Basin (modified after Qiao et al., 2023) and the studied well (Qi 1 well) location. The thickness of the Lucaogou Formation in the Tianchi area after Carroll and Wartes (2003), at the JJZG section after Sun et al. (2022) and in the Jimusaer Sag after Huang et al. (2020).

approximately 800 m at the JJZG section (Sun et al., 2022) and approximately 570 m in the studied area, and finally to approximately 300 m in the Jimusaer Sag (Huang et al., 2020) (Fig. 1c). Based on lithology, the Lucaogou Formation can be divided into two members. For the examined Qi 1 well, the lithology of the upper member (2198.00–2440.00 m) is mainly mudstone interbedded with conglomeratic sandstone and muddy siltstone, and of the lower member (2440.00–2762.00 m) is dominated by mudstone interbedded with dolomite, argillaceous dolomite, and calcareous dolomite as well as dolomitic mudstone and calcareous mudstone (Fig. 2). A similar assemblage in lithology can be observed in the Ji 251 well in the Jimusaer Sag (Fig. 2; Huang et al., 2020). The fact that the lower member of the Lucaogou Formation develops more dolomite fine-grained sediments which almost disappear in the upper member can be observed at the JJZG section (Sun et al., 2022) and in the Zk 1 well in the Santanghu Basin which is closely located to the southeast of the

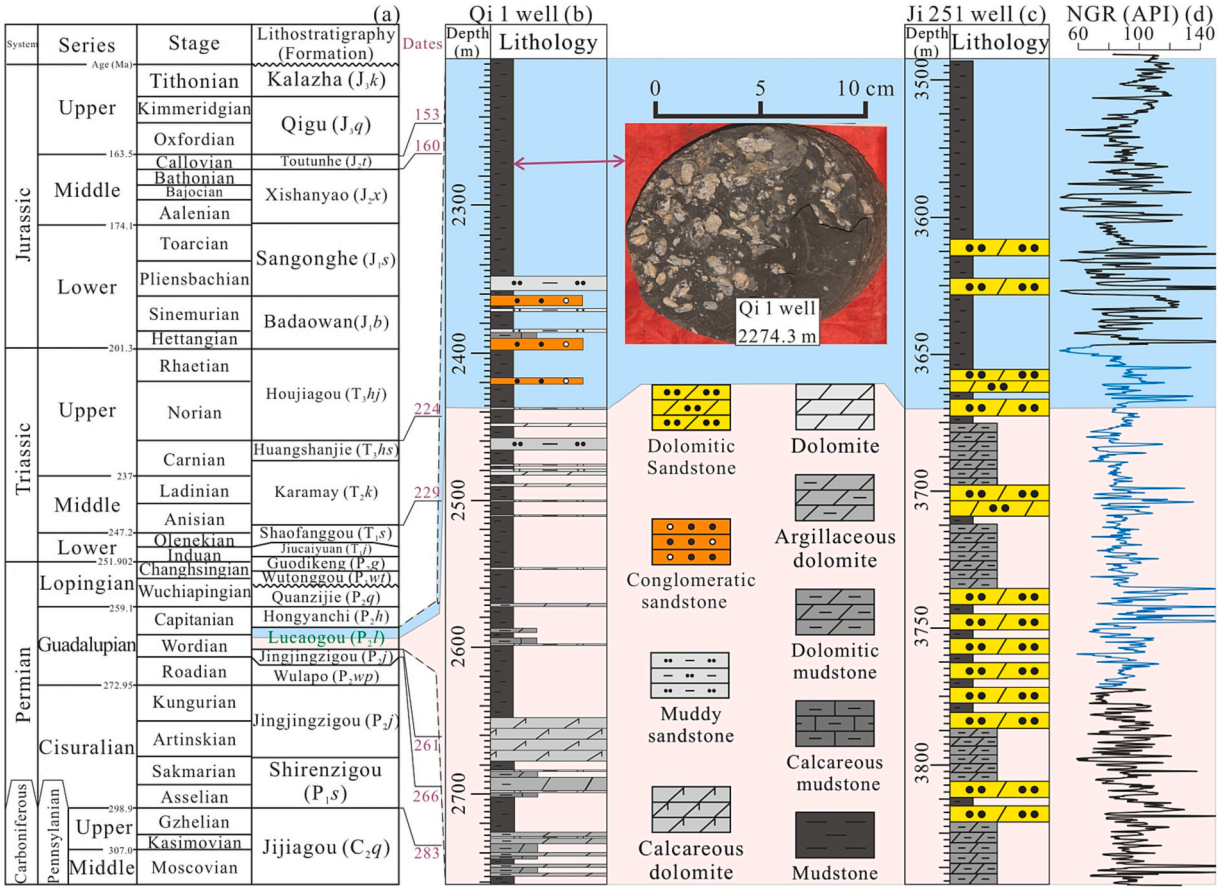

Fig. 2. (a) Permian-Jurassic stratigraphic column for the southern Junggar Basin, as well as the stratigraphic columns of the Lucaogou Formation in the (b) Qi 1 well and (c) Ji 251 well with (d) natural gamma ray. (a) modified after Zhao et al. (2020), (b) after Luo et al. (2018), and (c and d) after Huang et al. (2020).

Junggar Basin (Tao et al., 2017). This lithological assemblage was interpreted as a lacustrine environment (Carroll, 1998; Carroll and Wartes, 2003).

3. Methodology and samples

3.1. Samples and preparation

The preliminary petrographic and detailed organic geochemical characteristics from the Qi 1 well have been investigated by Luo et al. (2018). In this study, 24 and 40 drilling samples were used to investigate elemental composition and organic petrography, respectively, in detail. Before the measurements of major element oxides, trace and rare-earth elements, the samples were crushed to <200 mesh by using a tungsten carbide ball mill. For the organic petrography study, the samples cut from fresh drilling samples were broken into small particles, and then the epoxy resin was added and polishing them after horizontally laying for 24 h finally.

3.2. Analytical methods

3.2.1. Elemental analysis

The concentrations of major element oxides (units in wt%) and rest elements (i.e., trace elements and REEs; units in ppm) of the studied samples were analyzed using an ARL Perform' X 4200 wavelength-dispersive X-ray fluorescence (WD-XRF) spectrometer and an ELAN DRC-e inductively-coupled plasma mass spectrometer (ICP-MS), respectively. For the measurement of major element oxides concentrations, loss on ignition (LOI) was achieved by heating 1 g of the sample at 1100 °C for one hour. The analytical precision was better than 1%. For the measurement of trace elements and REEs concentrations, the sample of about 0.05 g was digested with a mixed solvent of hydrofluoric and nitric acids (V: V; 1: 1) in high-pressure Teflon bombs and then heated to 190 °C for 48 h. Internal and international standards (AGV-2, BCR-2, BH-VO2 and GSP-1 (USGS)) were used for calibration, and the precision was better than 5%. Three duplicates were analyzed to investigate the accuracy of the measurements which was better than 10%.

3.2.2. Organic petrography

The organic petrography studies related to the identification and quantification of maceral composition and measurement of vitrinite reflectance (VR_r) were carried out using a Leica DM4500P microscope. Group of liptinite was counted using a fluorescence light mode, and groups of inertinite and vitrinite were using a reflected white light mode. Classification and statistics of maceral composition were performed according to the description of the ICCP system 1994 (ICCP, 1998; ICCP, 2001; Pickel et al., 2017). The measurement of VR_r was performed by using a microscope photometer (MPV-SP), and about 50 random vitrinite particles were measured for each sample.

3.3. Data presentation

The enrichment factor (EF; Tribovillard et al., 2006), evaluating the degree of elemental depletion/enrichment, is calculated by the following equation:

$$X_{EF} = (X/Al)_{sample} \Big/ (X/Al)_{PAAS} \quad (1)$$

In which, X is the target element and PAAS is Post–Archean Australian Shale (Taylor and McLennan, 1985).

The Chemical Index of Alteration (CIA; Nesbitt and Young, 1982), measuring the relative concentrations of feldspars and their chemical alteration products (i.e., clay minerals) in sedimentary rocks/sediments, was used to evaluate weathering degree and paleoclimate condition in provenance area (Fedo et al., 1995; Qiao et al., 2022). It can be calculated via the A–CN–K (Al_2O_3–CaO* + Na_2O–K_2O) ternary diagram. In which, the CaO* referring to the CaO only in silicate fraction is calculated using the following equation:

$$CaO^* = CaO - 10/3 \times P_2O_5 \quad (2)$$

CaO* value is also adopted for the calculations of the WIP (Weathering Index of Parker; Parker, 1970) indicating weathering degree by estimating the contents of alkaline and alkali earth elements in weathered products (Parker, 1970) and M–F–W system (Mafic–Felsic–Weathering; Ohta and Arai, 2007) mentioned later.

In the CIA system, the proportion of Na_2O is used as the proportion of CaO* in the silicate fraction in the case of CaO* > Na_2O; while the CaO* is used in the case of CaO* ≤ Na_2O (Nesbitt and Young, 1982; Mclennan, 1993; Zhu et al., 2020).

The CIA and WIP values can be calculated using the following Eqs. (3 and 4), respectively:

$$CIA = Al_2O_3/(Al_2O_3 + CaO^* + Na_2O + K_2O) \times 100 \quad (3)$$

$$WIP = 100 \times (CaO^*/0.7 + 2 \times Na_2O/0.35 + 2 \times K_2O/0.25 + MgO/0.9) \quad (4)$$

where the oxides are molar concentrations.

The M–F–W diagram shows the least altered nature and weathering as well as sedimentary recycling trends. In which the M, F and W are calculated following the below equations:

$$\begin{aligned} M = &-0.395 \times ln(SiO_2) + 0.206 \times ln(TiO_2) - 0.316 \times ln(Al_2O_3) \\ &+ 0.160 \times ln(Fe_2O_3) + 0.246 \times ln(MgO) + 0.368 \times ln(CaO^*) \\ &+ 0.073 \times ln(Na_2O) - 0.342 \times ln(K_2O) + 2.266 \end{aligned} \quad (5)$$

$$\begin{aligned} F = &0.191 \times ln(SiO_2) - 0.397 \times ln(TiO_2) + 0.020 \times ln(Al_2O_3) \\ &- 0.375 \times ln(Fe_2O_3) - 0.243 \times ln(MgO) + 0.079 \times ln(CaO^*) \\ &+ 0.392 \times ln(Na_2O) + 0.333 \times ln(K_2O) - 0.892 \end{aligned} \quad (6)$$

$$\begin{aligned} W = &0.203 \times ln(SiO_2) + 0.191 \times ln(TiO_2) + 0.296 \times ln(Al_2O_3) \\ &+ 0.215 \times ln(Fe_2O_3) - 0.002 \times ln(MgO) - 0.448 \times ln(CaO^*) \\ &- 0.464 \times ln(Na_2O) + 0.008 \times ln(K_2O) - 1.374 \end{aligned} \quad (7)$$

Note that the oxides (units are in wt%) are normalized to 100 wt% before calculation. After that, the exponents of these three values are taken and re-normalized to 100.

The WIS (Weathering Intensity Scale; Meunier et al., 2013) is another indicator estimating the weathering intensity via combining the accumulation of immobile elements (e.g., Fe and Al) and loss of silica, which is based on the M^+–4Si–R^{2+} system considering monocationic millimoles (i.e., number of cations) from oxide amounts,

$$\text{where } 4Si = \text{mMol Si}/4 \quad (8)$$

$$R^{2+} = \text{mMol } Mg^{2+} + \text{mMol } Mn^{2+} \quad (9)$$

$$M^+ = \text{mMol } Na^+ + \text{mMol } K^+ + 2 \times \text{mMol } Ca^{2+} \quad (10)$$

The Index of Compositional Variability (ICV) which was used to evaluate compositionally maturity can be calculated by the following equation proposed by Cox et al. (1995):

$$ICV = (Fe_2O_3 + K_2O + Na_2O + CaO + MgO + MnO + TiO_2)/Al_2O_3 \quad (11)$$

The Sodium Depletion Index (τNa; Rasmussen et al., 2011), another weathering index, can be calculated by the following equation:

$$\tau Na = \left[(Na/Zr)_{sample} \Big/ (Na/Zr)_{detrital} - 1 \right] \quad (12)$$

where $(Na/Zr)_{sample}$ represents the Na/Zr ratio in the studied samples, and $(Na/Zr)_{detrital}$ takes 152.11 based on the average related elements' concentrations of the upper continental crust (UCC) (McLennan, 2001).

Biogenic elements, e.g., silica (Si_{bio}), barium (Ba_{bio}) and phosphorus (P_{bio}), can be used to evaluate paleoproductivity, which can be calculated using the following equation proposed by Schoepfer et al. (2015):

$$X_{bio} = X_{sample} - \left[Al_{sample} \times (X/Al)_{detrital} \right] \quad (13)$$

where X_{bio} and X_{sample} represent the biogenic and total concentration of the target element, respectively, and Al_{sample} represents the total concentration of Al in the studied samples. In this study, $(Si/Al)_{detrital}$, $(P/Al)_{detrital}$ and $(Ba/Al)_{detrital}$ are taken to be 3.83, 0.0087 and 0.0068, respectively, based on the average related elements' concentrations of the UCC (McLennan, 2001).

4. Results

4.1. Major element oxides

Fig. 3a shows the concentrations of the major element oxides normalized to PAAS values. The concentrations and related parameters used in this study are listed in Table 1 (all tables mentioned are given in the Appendix). Compared with PAAS values, the Lucaogou Formation are slightly depleted in SiO_2, TiO_2, Al_2O_3, Fe_2O_3, and K_2O, while slightly enriched in Na_2O and P_2O_5 as well as significantly enriched in CaO (Fig. 3a). The concentrations of MgO and MnO vary around PAAS values (Fig. 3a).

The log plot of (Fe_2O_3/K_2O) (0.07–0.59) vs. (SiO_2/Al_2O_3) (0.64–0.89) (Table 1) shows that the studied samples fall in the typical field of Fe-shale (Fig. 4a; Herron, 1988). In addition, the depletion in SiO_2 indicates a non-marine environment for the studied samples because the high biogenic silica content leads to SiO_2 being enriched in marine shales (Ross and Bustin, 2009). The lacustrine environment can be demonstrated by the Nestoria fossils (Fig. 2) as well. The K_2O/Al_2O_3 ratios are 0.14–0.30 (0.21 on average) and elemental Al/Si are 0.14–0.20 (avg. 0.18), respectively (Table 1). The CIA and WIP values for the studied samples are 46.14–64.22 (avg. 55.42) and 33.38–86.89 (58.64 on average), respectively (Table 1). Moreover, the ICV and τNa values range from 1.25 to 3.50 (avg. 1.74) and from −0.68 to −0.36 (avg. −0.54), respectively (Table 1).

4.2. Rare-earth elements

REEs concentrations in sediments are generally normalized to classic sedimentary rocks, such as the UCC (e.g., Dai et al., 2014) and PAAS (e.g., Tao et al., 2017), and to chondrite (e.g., Cullers, 1995; McLennan et al., 1990; Dai et al., 2011) due to sediments recording the characteristics of both provenance origin and chemical alteration products (Dai et al., 2016). Fig. 3b shows PAAS–normalized distribution patterns of the REEs, which are characterized by slightly increasing REE distributions from La to Lu, but positive Eu anomalies (Eu_{anom}) (Fig. 3b).

The ΣREE concentrations range from 70.20 to 150.21 ppm (Table 2) and are depleted compared to PAAS values. The La/Yb and La_n/Yb_n (subscript n represents PAAS–normalized value) are 6.65–10.59 and 0.45–0.72, respectively (Table 2). Rock types of the studied samples are analyzed using the plot of ΣREE vs. La/Yb, indicating all sample data are plotted into the intersection field of calcareous mudstones, alkaline basalts and continental tholeiites (Fig. 4b). The Eu_{anom} values, calculated via $Eu_N/(Sm_N \times Gd_N)^{1/2}$ (subscript N represents chondrite–normalized value), are 0.62–0.79 with an average value of 0.73 (Table 2).

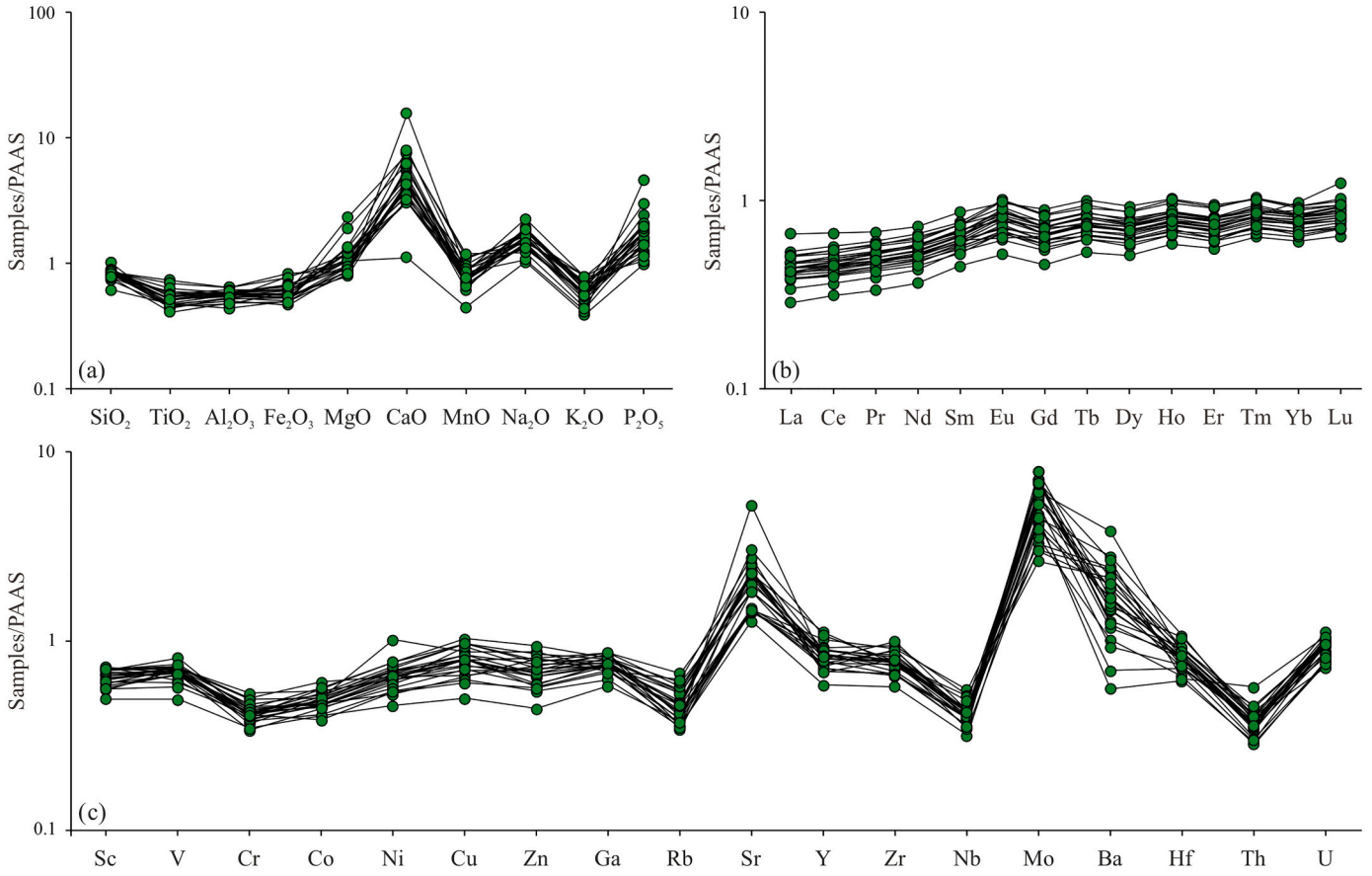

Fig. 3. Distribution patterns of PAAS–normalized (a) major element oxide, (b) rare-earth element and (c) trace element of the Middle Permian Lucaogou oil shale from the Qi 1 well located in the southern Junggar Basin, China.

4.3. Trace elements

Relative to PAAS values, the studied samples show that only Sr and Mo are significantly enriched, Ba shows a large variation, and the rest trace elements including Sc, V, Cr, Co, Ni, Cu, Zn, Ga, Rb, Y, Zr, Nb, Hf, Th and U are slightly depleted (Fig. 3c). Mo_{EF} and U_{EF} values range from 2.13 to 8.13 (avg. 4.95) and from 1.45 to 2.34 (avg. 1.66), respectively (Table 3). Th and Zr concentrations in comparison to Sc concentrations are 0.35–1.05 and 11.87–20.44, respectively (Table 3). Co and Cr concentrations compared to Th concentrations range from 1.11 to 2.69 and from 4.58 to 10.45, respectively (Table 3). The trace elements concentrations and their related parameters used in this study, i.e., ratios of Cr/V (0.36–0.54), Y/Ni (0.28–0.93), Nb/Y (0.25–0.39), Ni/Co (2.57–4.89), V/(V + Ni) (0.66–0.78), and Cd/Mo (0.02–0.13), as well as Co × Mn (0.45–1.33), are listed in Table 3.

4.4. Maceral composition and vitrinite reflectance

The dominant maceral is mineral-bituminous groundmass with the volumetric percentage ranging between 30% and 88% (avg. 74%; Table 4). This maceral is a mixture of amorphous fine granular inorganic-organic matter, showing brightly yellow fluorescence under fluorescent light (Fig. 5 a, b, c, d; Luo et al., 2018). This maceral was regarded as amorphinite, amorphous OM, or bituminite in previous studies (cf. Fishman et al., 2012; Ma et al., 2015; Hackley et al., 2016). The following maceral is vitrinite (volumetric percentage being 10–55%; avg. 21%) with VR_r ranging from 0.75% to 0.85% (0.80% on average) and the standard deviation of 0.06–0.10 (0.08 on average) (Fig. 5e, f, g and h; Table 4). The abundance of inertinite (e.g., fusinite particles) is few in all samples (Fig. 5e, f, g and h), accounting for volumetric percentages between 2% and 10% (3% on average) of the total macerals counted (Table 4). The rest maceral composition is alginite including prasinophyte green algae (i.e., telalginite; Fig. 5a, b and c), lamalginite and liptodetrinite (Fig. 5b), being 0–10% (avg. 1%) in volumetric percentage (Table 4). Pyrites are rare in all samples occurring either as euhedral crystals (Fig. 5e, f and g) or as assemblages of recrystallized framboidal pyrite with diameters > 20 μm in most cases (Fig. 5h).

5. Discussion

5.1. Provenance and paleotectonic setting

The provenance of sedimentary rocks/sediments is assemblage including sedimental, metamorphic, and/or igneous rocks, and the geochemical composition of sedimentary rocks/sediments is mainly determined by which they were derived (McLennan et al., 1993). Some trace elements and REEs are stable in the processes of transport and sedimentation and thereby were successfully used to determine sediment provenance (Taylor and McLennan, 1985; McLennan, 1989; McLennan and Taylor, 1991; McLennan et al., 1993).

Zr is more easily to be enriched during the deposition process because it is mostly concentrated in zircon which is resistant to erosion and chemical weathering. In addition, Th and Sc can be used to evaluate sediment provenance, because Sc and Th which are showing little fractionation during the sedimentary cycle are enriched in mafic and felsic rocks, respectively (Feng and Kerrich, 1990; McLennan et al., 1990). So, the Th/Sc vs. Zr/Sc diagram was used to interpret compositional variations and sediment recycling (Fig. 6a; McLennan et al., 1993). In first–cycle sediments (line A in Fig. 6a), the Th/Sc ratio is positively related to Zr/Sc ratio which is a proxy of heavy mineral

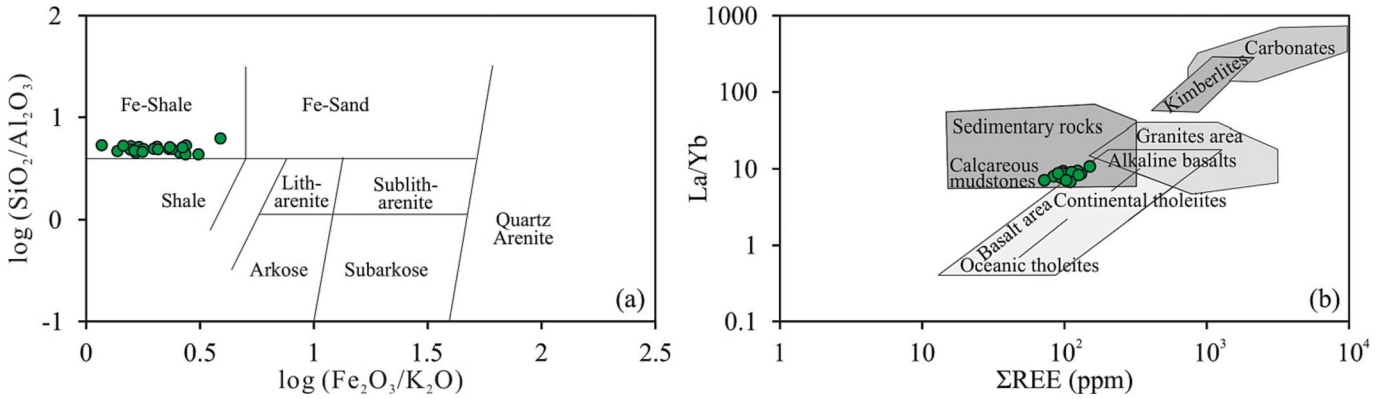

Fig. 4. Diagrams of (a) log (Fe_2O_3/K_2O) vs. log (SiO_2/Al_2O_3) (after Herron, 1988) and (b) La/Yb vs. ∑REE (after Allègre and Michard, 2012) illustrating rock types.

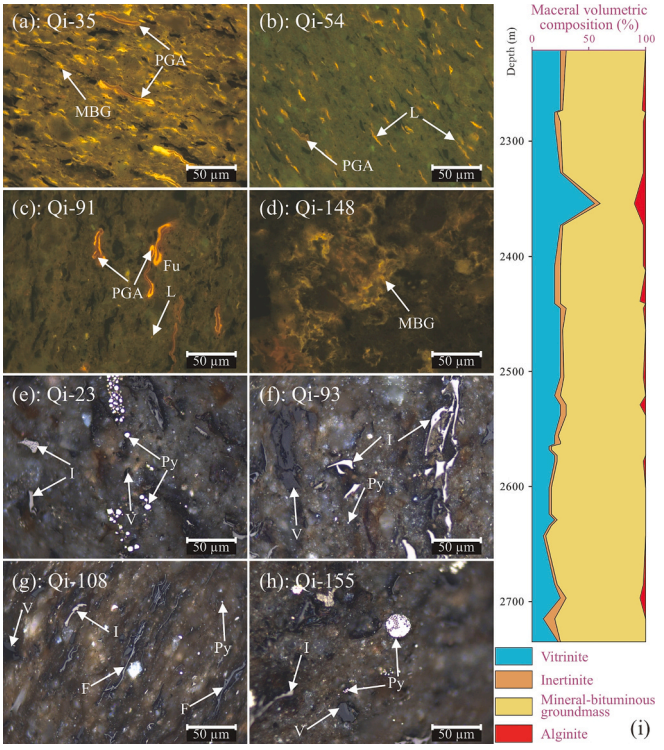

Fig. 5. Photomicrographs representative of the organic matter and pyrite under (a, b, c, d) fluorescence and (e, f, g, h) incident white light mode, as well as (i) maceral compositions of the Middle Permian Lucaogou oil shale from the Qi 1 well located in the southern Junggar Basin. Showing prasinophyte green algae/telalginite (PGA in a, b and c), lamalginite/liptodetrinite (L in b and c), mineral-bituminous groundmass (MBG in a and d), vitrinite (V in e, f, g, and h), pyrite (Py in e, f, and h), fusinite (F in g), and inertinite (I in e, f, g, and h). (For interpretation of the references to colour in this figure legend, the reader is referred to the web version of this article.)

concentration (Taylor and McLennan, 1985; McLennan, 1989), indicating the original composition of the provenance. In contrast, the sediment cycling or more mature sediments (line B in Fig. 6a) show a large variation in Zr/Sc ratios but little variation in Th/Sc ratios (McLennan et al., 1993). Sedimentary recycling can incorrectly convey information that more intense weathering conditions (Garzanti et al., 2013). The lower REE concentrations in the investigated shales in comparison to those in PAAS suggest the recycling process in PAAS was probably more intense (Fig. 3b). Fig. 6a illustrates that the Lucaogou samples were not affected by recycling sediments, so they can be used to identify provenance (Wu et al., 2022) and paleoclimate conditions. No recycling sediments is also supported by no enrichment of quartz (Fig. 6b; Garzanti et al., 2013), and by the high ICV values of >1 which indicates compositional immaturity of the studied samples and active tectonic scenery (Table 1; Cox et al., 1995; Cullers and Berendsen, 1998).

The Eu_{anom} is negative in felsic-intermediate rocks, while little or no negative in mafic rocks when it is normalized to chondrite (Cullers et al., 1987; Cullers, 1995; Dai et al., 2016). Moreover, Eu_{anom} shows positive values in mafic rocks, but negative in felsic rocks in the case that it is normalized to the UCC values (Dai et al., 2014; Dai et al., 2018). The Eu_{anom} vs. Th/Sc plot indicates that the analyzed samples fall into the fields of mafic and granitoid sources without any amphibolite source (Fig. 7a; McLennan et al., 1990; Cullers, 2002). Moreover, the Eu_{anom} value in the studied samples is greater than that in PAAS (i.e., positive Eu_{anom} in the case that it is normalized to PAAS) which was derived from a granitoid source (Taylor and McLennan, 1985), showing the studied samples should have more terrigenous material derived from a mafic source in relation to PAAS (Fig. 7a). In comparison to the UCC value in Fig. 7a, the studied samples were derived from mixed felsic/mafic sources. However, in some cases, Eu values cannot be accurately measured by using the ICP-MS technique during the analyses of sedimentary rocks, because some elements, especially Ba, show significant interference with Eu measurement (Dai et al., 2016). Yan et al. (2018) argued that Eu_{anom} is accurate only if Ba/Eu is <1000, otherwise, Eu_{anom} is overvalued. In this study, the Ba/Eu values ranging between 384.24 and 2060.33 (Table 5) indicate that most Eu_{anom} values are likely interfered by Ba concentrations. The Eu_{anom} values in samples with Ba/Eu > 1000 are slightly higher than those in samples with Ba/Eu < 1000 and the UCC. The interference leads to the provenance containing more mafic rocks in the evaluation results in the case that the Eu_{anmo} is normalized to the UCC. However, the interference is limited and does not affect the results evaluated when the Eu_{anom} is normalized to chondrite values (Fig. 7a). To sum up, the provenance was derived from felsic-intermediate rocks.

The bivariate diagram of La/Th (2.36–5.54; Table 5) vs. Hf is also a useful indicator to distinguish felsic and mafic composition-dominated arcs (Floyd and Leveridge, 1987), which shows that 23 out of 24 samples plot in the field of mixed felsic/mafic sources (Fig. 7b). A similar result can be corroborated by the bivariate plots of La/Sc (1.27–2.63; Table 5) vs. Co/Th and Cr/Th vs. Sc/Th, indicating that the analyzed samples were derived from felsic to intermediate sources (e.g., granodiorite and andesite) (Fig. 8a and b). This result is consistent with the plots of Y/Ni vs. Cr/V illustrating insignificant input from mafic-ultramafic and felsic sources (Fig. 8c) and of Nb/Y vs. Zr/TiO_2 (0.03–0.04; Table 5) indicating the studied samples are geochemically located around the boundary between andesite and rhyodacite/dacite (Fig. 8d). The provenance derived from felsic to intermediate sources (e.g., granodiorite, andesite and dacite) without recycling sediments can also be corroborated by the triangular diagrams of M–F–W (Fig. 9a),

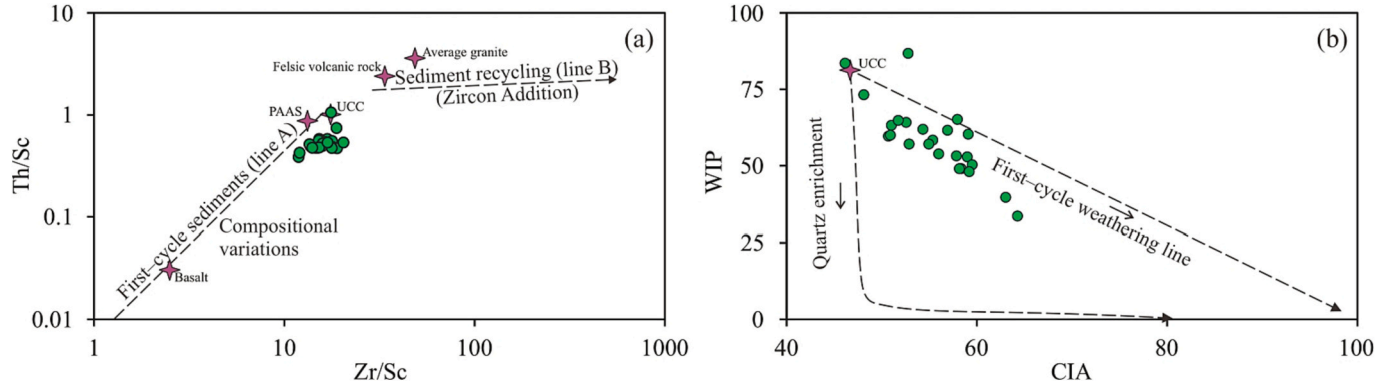

Fig. 6. (a) Th/Sc vs. Zr/Sc (modified after McLennan et al., 1993) and (b) WIP vs. CIA (modified after Garzanti et al., 2013) illustrating weathering and sediment recycling.

M^{+}–4Si–R^{2+} (Fig. 9b) and Rb/V–Zr/Zn–Sc/Nb (Fig. 9c; Sawant et al., 2017) (Table 5). In the calculation process of the M^{+}–4Si–R^{2+} system, the R^{2+} is calculated without Fe^{2+} content because only total Fe is measured during chemical analysis. However, this uncertainty cannot affect the results in this study because it is important for mafic and ultramafic rocks but is not significant for shales, granite, graywackes or granodiorite (Meunier et al., 2013).

The tectonic setting discrimination diagrams based on major element oxides were proposed by Bhatia (1983) as well as Roser and Korsch (1986). However, these discrimination plots have received considerable criticism (Ryan and Williams, 2007). Generally, tectonic settings can be divided into passive and active continental margins, as well as oceanic and continental island arcs (Bhatia, 1983). Some trace elements (e.g., Th, Sc and Zr) and REEs (e.g., La) have a relatively short residence time and low mobility in water columns (LaMaskin et al., 2008). So, paleotectonic settings of sedimentary basins can be determined by the diagrams based on the relative distributions of these elements (Bhatia and Crook, 1986). The paleotectonic setting of the Junggar Basin during the deposition of the Lucaogou Formation was a continental island arc domain, which is supported by the ternary diagrams of La–Th–Sc, Th–Cs–Zr/10 and Th–Co–Zr/10 (Fig. 10a, b and c; Table 5). In addition, the samples are also distributed in the field of continental island arc in the Ti/Zr vs. La/Sc plot (Bhatia and Crook, 1986) (Fig. 11).

Briefly, the provenance of the studied samples was derived from felsic to intermediate sources (e.g., granodiorite, andesite and dacite) without contributions of ancient crustal sedimentary rocks/sediments. Considering the tectonic evolution of the basin, the provenance might source from the Middle-Late Permian continental foreland basin. It is unlikely that the provenance came from the Bogda Mountains, given that it was a receptive deposit during the Paleozoic period (Wang et al., 2018). The major and minor provenances of the sedimentary rocks in the Bogda Mountains range were the North and Central Tianshan Mountains, respectively, during this period (Wang et al., 2018; Zhao et al., 2020).

5.2. Paleoclimate and weathering

Paleoclimates control terrigenous materials inputs, lake water levels, and aqueous environments (e.g., water chemistry, salinity and redox conditions) as well as species and growth rates of plants in drainage areas by controlling chemical weathering intensity and ecosystem, thereby exerting effects on organic and mineral compositions of OM-rich sediments (Nesbitt and Young, 1982; Fedo et al., 1995; Meyers, 1997; Ross and Bustin, 2009; Kemp et al., 2016; Song et al., 2018; Qiao et al., 2021a and b).

Chemical weathering indices are affected by siliciclastic sedimentary sorting caused by hydraulic effect via modifying the mineral/elemental composition of sediments (Galy et al., 2008; Garzanti et al., 2010, 2011; Garzanti et al., 2013; Bouchez et al., 2011; Lupker et al., 2012; Laceby et al., 2017). For instance, hydraulic sorting effects are negatively related to both WIP and τNa because the calculations of WIP and τNa are based on hydraulic sorting sensitive elements, i.e., alkali metals and zircon, respectively (Garzanti et al., 2013). So, values of WIP, τNa and CIA are lower in coarser-grained than those in finer-grained sediments under the same provenance and weathering conditions (Garzanti et al., 2013; Jian et al., 2013; Guo et al., 2018). In this study, all the studied samples were collected from fine-grained layers which are little affected by the hydraulic sorting effect in relation to coarse-grained sedimentary rocks/sediments (McCulloch and Wasserburg, 1978; Bhat and Ghosh, 2001). Hydraulic sorting can be evaluated by Al/Si ratio which is

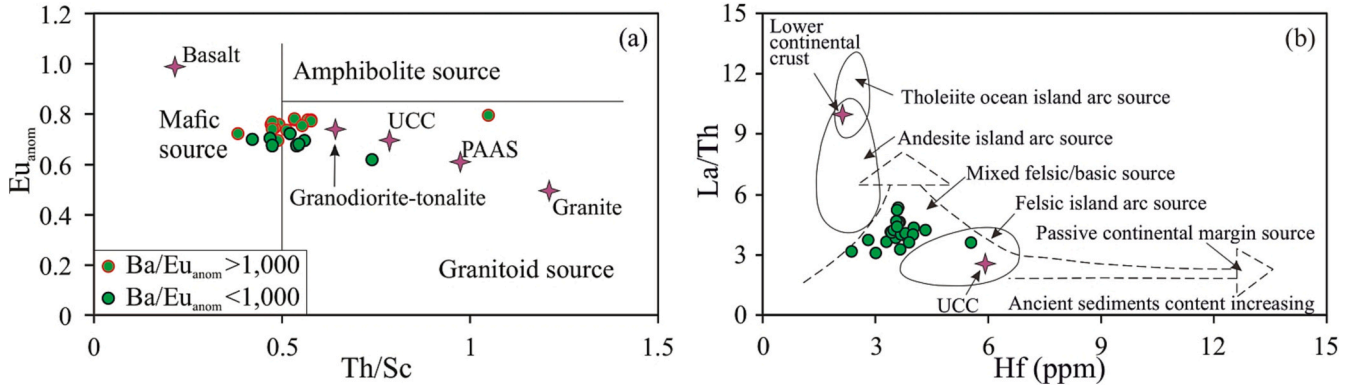

Fig. 7. (a) Th/Sc vs. Eu_{anom} and (b) La/Th vs. Hf (modified after Floyd and Leveridge, 1987) for sediment discrimination, illustrating the principal types of rocks. Eu_{anom} is calculated via $Eu_N/(Sm_N \times Gd_N)^{1/2}$.

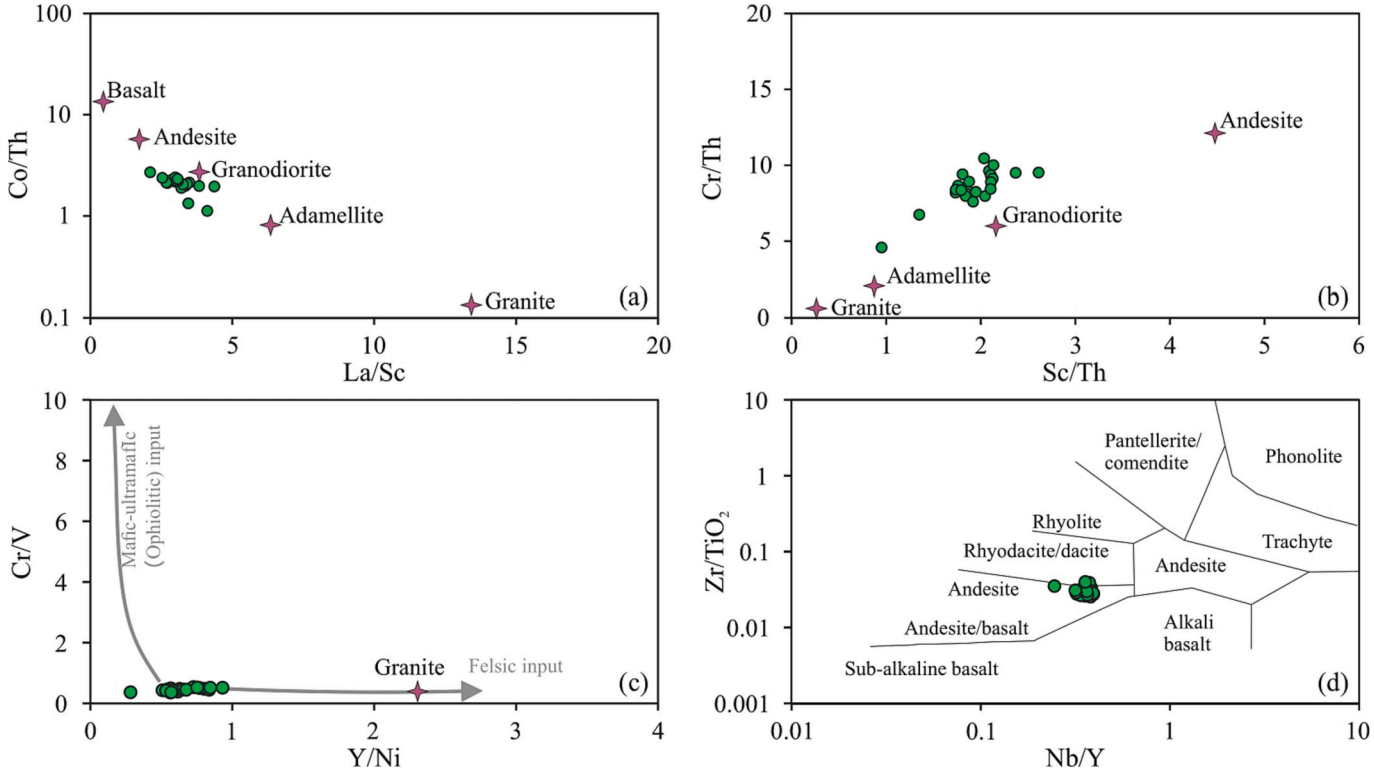

Fig. 8. (a) La/Sc vs. Co/Th (after Condie, 1993), (b) Cr/Th vs. Sc/Th (after Condie and Wronkiewicz, 1990), (c) Cr/V vs. Y/Ni (after Mongelli et al., 2006), and (d) Nb/Y vs. Zr/TiO_2 (after Winchester and Floyd, 1977) diagrams, showing the principal types of rocks.

negatively related to grain size because Al is mainly hosted in clay minerals in fine-grained sedimentary rocks/sediments and Si concentration indicates the coarser fraction (i.e., feldspar and quartz) (Galy et al., 2008; Bouchez et al., 2011; Lupker et al., 2012). For the studied samples, there is no clear relationship between the Al/Si ratio and either τNa or WIP (Fig. 12), indicating that sedimentary sorting shows little effect on fluctuation in weathering indices. Moreover, Ti can be trapped by new-formed clay minerals and concentrated in resistant coarse heavy terrigenous detritus, but Zr is only concentrated in coarse heavy minerals of terrigenous detrital inputs (Malengreau et al., 1995; Bouchez et al., 2011; Greber and Dauphas, 2019). Ti/Al ratio is a reliable parameter for deposition rate and siliciclastic grain size, i.e., a lower Ti/Al ratio indicates a lower deposition rate and a smaller grain (Bertrand et al., 1996; Caplan and Bustin, 1999; Murphy et al., 2000). The low deposition rate, fine-grained size, and the truth that hydraulic sorting exerts little effect on the chemical composition of the studied samples can be further supported by the non-negative relationship between Th and either Ti or Zr (Fig. 12c and d) (Zhao and Zheng, 2015), the low Ti/Al ratios, and Ti being positively correlated to Al but poorly correlated to Zr.

Generally, CIA values of <70 indicate weak chemical weathering linking arid/cold conditions, 70–80 indicate middle chemical weathering linking warm and humid conditions, and > 80 mean strong chemical weathering linking hot and humid conditions (Fig. 13a; Nesbitt

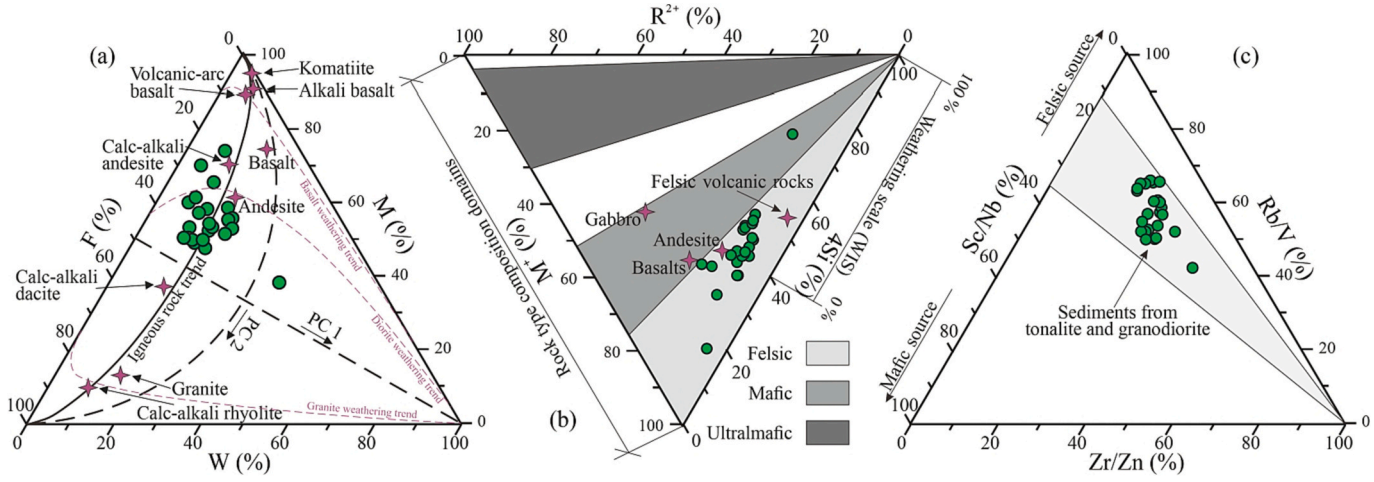

Fig. 9. Triangular diagrams of (a) Mafic (M)–Felsic (F)–Weathering (W), (b) M^{+}–4Si–R^{2+} (after Meunier et al., 2013), and (c) Rb/V–Zr/Zn–Sc/Nb (after Sawant et al., 2017), showing the principal types of rocks and weathering scale. (a) showing the least altered nature (PC 2) as well as weathering and sedimentary recycling trends (PC 1) (pattern and MFW index are calculated using major element oxides after Ohta and Arai, 2007).

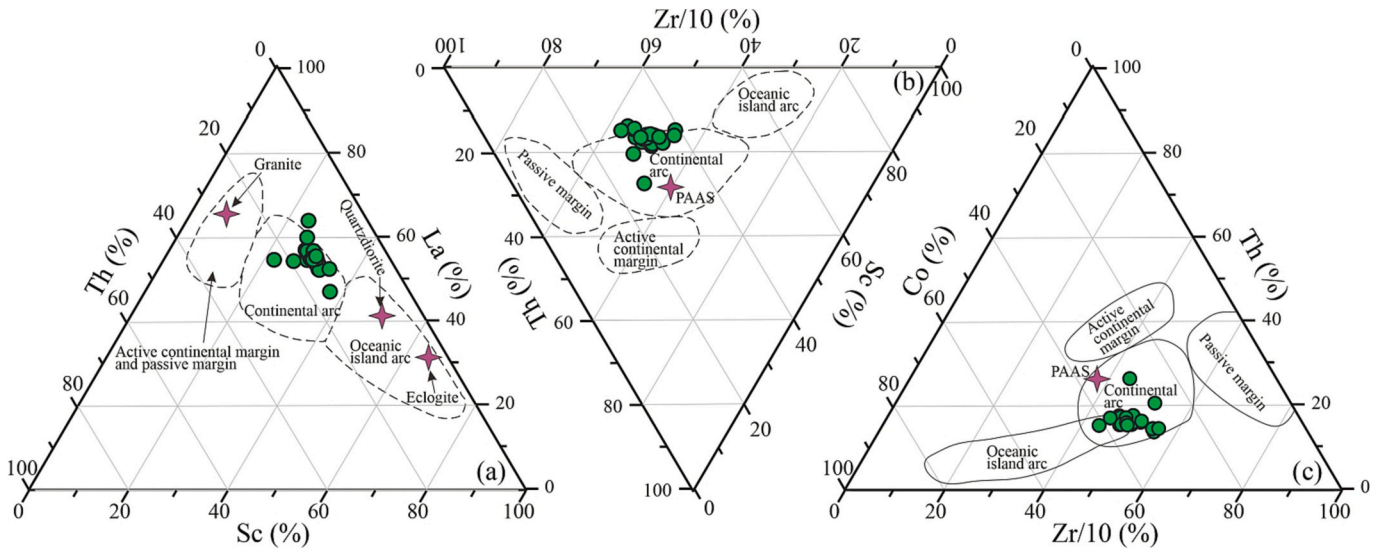

Fig. 10. Discrimination diagrams of (a) La–Th–Sc, (b) Th–Sc–Zr/10 and (c) Th–Co–Zr/10 (after Bhatia and Crook, 1986), illustrating the tectonic setting.

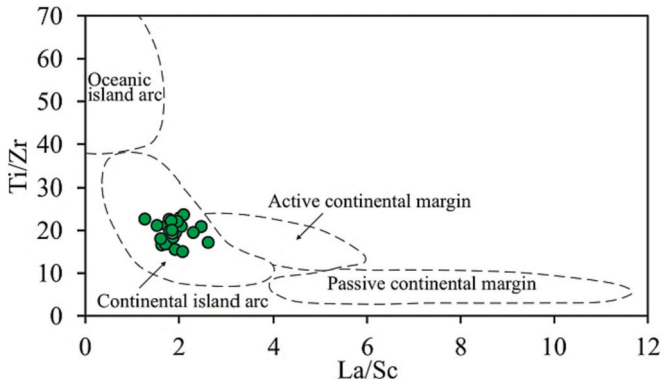

Fig. 11. (a) Ti/Zr vs. La/Sc diagram showing fields for tectonic settings (after Bhatia and Crook, 1986).

and Young, 1982). The CIA values should be corrected due to the possible effects of diagenesis and K-metasomatism (Nesbitt and Young, 1984; Fedo et al., 1995). The correction procedure of CIA values is referred to after Qiao et al. (2022) in detail via the A–CN–K ternary diagram. The best-fit metasomatic trend through the studied samples (dashed line with arrow A, Fig. 13a) intersected with the line of plagioclase–K-feldspar join represents the unweathered provenance rocks' proportion closing to granodiorite, which is consistent with the above provenance result. The CIA values of the studied samples indicate arid and cold paleoclimate conditions with weak chemical weathering. The weak chemical weathering is also in accord with the low weathering index (W) (Fig. 9a; Ohta and Arai, 2007) and WIS values (Fig. 9b; Meunier et al., 2013), as well as the high τNa and WIP values. The arid and cold paleoclimate conditions are further confirmed by the boundary binary diagrams of Ga/Rb vs. K_2O/Al_2O_3 (Fig. 13b; Roy and Roser, 2013; Qiao et al., 2022) and of $Al_2O_3 + K_2O + Na_2O$ vs. SiO_2 (Fig. 13c). It should be noted that all paleoclimate proxies show an episode with a warming/enhanced continental weathering trend (Fig. 14b-f). Similar CIA and WIP trends were observed at the JJZG section, but they indicate the upper member suffered warm and humid paleoclimatic conditions in the later stage (Cheng et al., 2022; Sun et al., 2022). The different CIA values between this study and previous studies may be due to outcrops having experienced more weathering. Lowry et al. (2014) argued that atmospheric pCO_2 might be the primary controlling factor on the Late Paleozoic continental-scale glaciation in comparison to solar irradiance and paleogeographic configurations. Increasing atmospheric pCO_2 leads to the increase of the surface temperature and thereby promotes the silicate weathering intensity due to the intensified hydrologic cycle and ocean acidification (Gernon et al., 2021; Deng et al., 2022). Considering the increases in atmospheric pCO_2 from Sakamarian to Artinskian Stage and during Guadalupian Series on global-scale (Qie et al., 2019; Zhang and Torsvik, 2022), the enhanced chemical weathering intensity might be because of the increase in atmospheric pCO_2. The enhanced chemical weathering intensity was also possibly caused by the continuously heightening denudation provenance area, i.e., the North and Central Tianshan Mountains (Zhao et al., 2020).

The stable variations in the La_n/Yb_n ratios which are regarded as an indicator of deposition rate (e.g., Zhang et al., 2013), Ti/Al and Al/Si ratios as well as Al and Ti concentrations show stable terrigenous detrital input, deposition rate, and transport distance during this warming and/or enhanced continental weathering episode (Fig. 14h-i). Meanwhile, the stable OM contents (Fig. 14a) and maceral composition (Fig. 5i), as well as relatively low concentrations of resins + asphaltenes (from 41.4 to 70.9% and 57.1% on average, of EOM) and saturate/aromatic hydrocarbon ratios (from 0.85 to 1.98%; avg. 1.37%) (Fig. 14m and n) indicate that the higher plant detritus inputs were limited over the studied stage due to the cold/arid paleoclimate conditions. The limited OM input from terrigenous higher plants is consistent with the evidence from biomarkers and Rock-Eval data that Luo et al. (2018) reported.

5.3. Paleoenvironment conditions

5.3.1. Paleosalinity

In lake systems, salinity shows an important role in the community composition of aquatic organisms (Romero-Viana et al., 2012; Qiao et al., 2021a). Luo et al. (2018) argued that the studied samples were formed under a saline environment supported by the high β-carotane/n-alkane of the highest concentration (0.08–0.60) and high concentration of gammacerane index (GI) of 4.24–22.05%.

Generally, Sr/Ba ratio is a common indicator of salinity. In freshwater environments, these two elements exist as soluble bicarbonates. By contrast, Ba precipitates into $BaSO_4$ in water columns with high salinity, while Sr concentrations show little change (Wei and Algeo, 2020). Based on Sr/Ba ratio, Wei and Algeo (2020) proposed the thresholds for freshwater conditions (< 0.2), brackish water conditions (0.2–0.5) and marine water conditions (> 0.5). According to this principle, the Sr/Ba ratios of the studied samples indicate brackish to

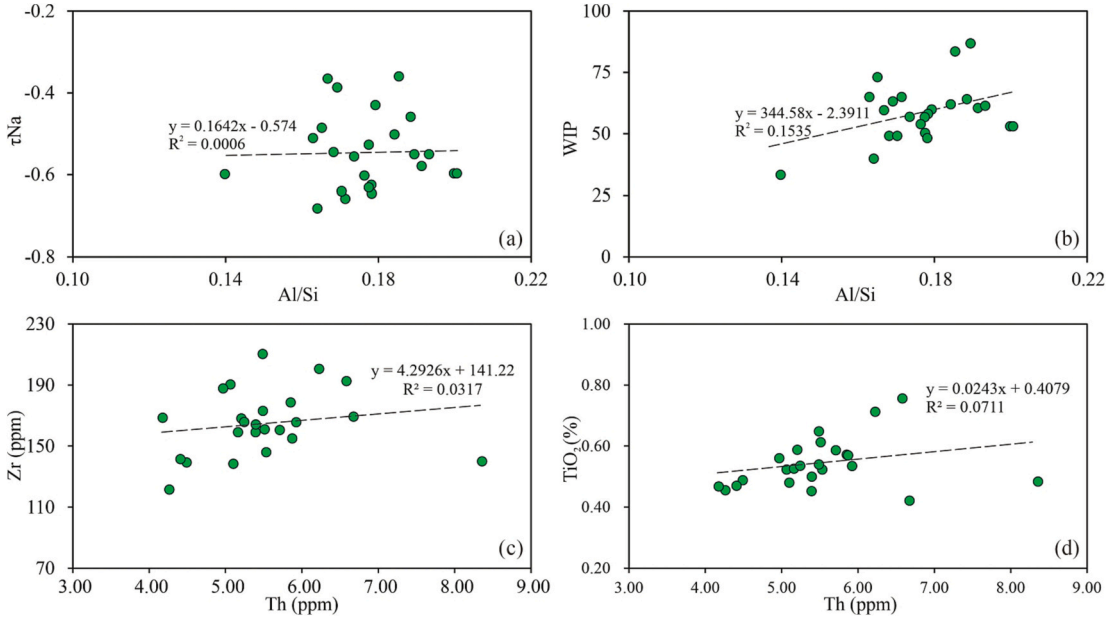

Fig. 12. Plots of Al/Si ratio (i.e., grain size and hydraulic sorting proxy) vs. (a) Sodium Depletion Index (τNa) and (b) Weathering Index of Parker (WIP) as well as Th vs. (c) Zr and (d) TiO_2, illustrating hydraulic sorting effect.

hypersaline conditions (Fig. 16b). In addition, Ga is mainly derived from feldspathic silicate and quartzose rocks, which is easily adsorbed by clay minerals, thereby resulting in enriched Ga concentrations in freshwater sediments (about 18–23 ppm) as compared with that in marine sediments (< 15 ppm) (Chen et al., 1997; Salminen et al., 2005; Breiter et al., 2013). The lower Ga concentrations of the studied samples are reversely related to Sr/Ba ratios, indicating a similar paleosalinity environment as well (Fig. 16b and c). It should be noted that the Sr/Ba ratios in the upper member (0.18–1.01 with an average value of 0.36) are smaller than those in the lower member (0.25–0.76 with an average value of 0.47), which indicates that the paleosalinity during the deposition of the upper member was lower than that during the lower member (Fig. 16b). More freshwater inputs in the upper member can be inferred from the biomarkers of the GI values (4.24–7.97 with an average value of 6.04 in the upper member and 7.97–42.21 with an average value of 21.58 in the lower member) and *β*-carotane/*n*-alkane of the highest concentration values which are 0.06–0.18 (avg. 0.14) in the upper member and are 0.18–0.45 (avg. 0.35) in the lower member. Considering the evolution of the paleoclimate conditions, the evaluation characteristics of the salinity parameters might be due to more rainfall caused by intensified hydrologic cycle. The higher *β*-carotane/*n*-alkane of the highest concentration values in the lower member also indicate more arid paleoclimate conditions (Peters et al., 2005). The difference in salinity between the upper and lower members is consistent with the existence of Nestoria fossils in the upper member (Fig. 2) and the lithological assemblage in which the lower member develops more dolomitic sediments which almost disappears in the upper member (Fig. 2).

5.3.2. *Paleoredox conditions*

Besides paleosalinity, OM preservation is affected by paleoredox conditions. A reducing environment was interpreted by Luo et al. (2018) based on the plot of pristane/*n*-C_{17} vs. phytane/*n*-C_{18} and pristane/phytane ratios as well as the high concentration of dibenzothiophene (DBT) in comparison with that of fluorene and dibenzofuran. Additionally, the low DBT/phenanthrene (PHE) of <0.1 (Luo et al., 2018) indicates no persistent and extensive H_2S in the benthic water column. Considering the related biomarker ratios, the paleoredox conditions can be further interpreted as least-reducing, i.e., suboxic (Tribovillard et al., 2012), environment.

The suboxic condition is also corroborated by the poor positive relationship between the TOC (total organic carbon) and Mo contents (Fig. 15a). This is because Mo can be easily sorbed by OM in the environment with persistent H_2S, thereby showing a clear positive relationship between them (Helz et al., 1996; Tribovillard et al., 2012).

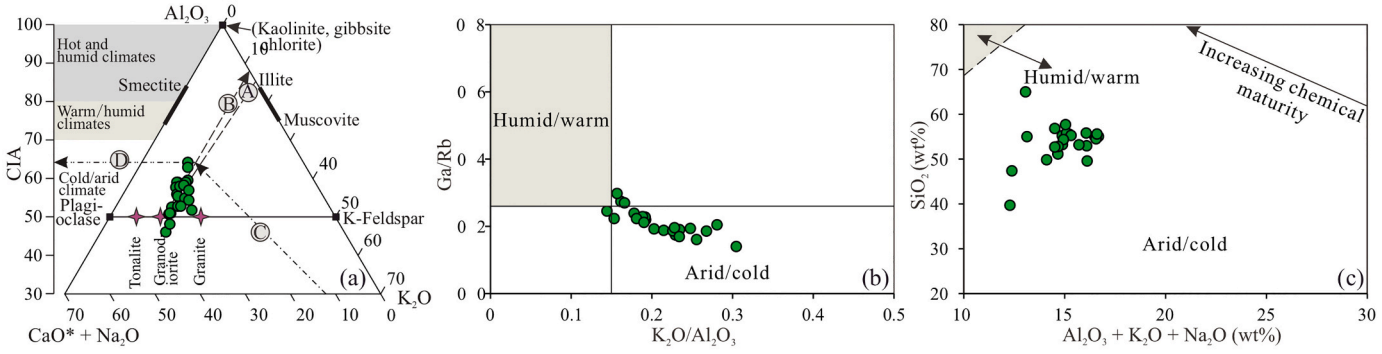

Fig. 13. (a) A–CN–K ternary diagram for mudstone correction for K metasomatism is made by projecting data points back onto the ideal weathering pathway from K-apex (after Fedo et al., 1995), as well as discrimination diagrams of (b) Ga/Rb vs. K_2O/Al_2O_3 (after Qiao et al., 2022) and (c) SiO_2 vs. ($Al_2O_3 + K_2O + Na_2O$) (after Suttner and Dutta, 1986), indicating paleoclimate conditions.

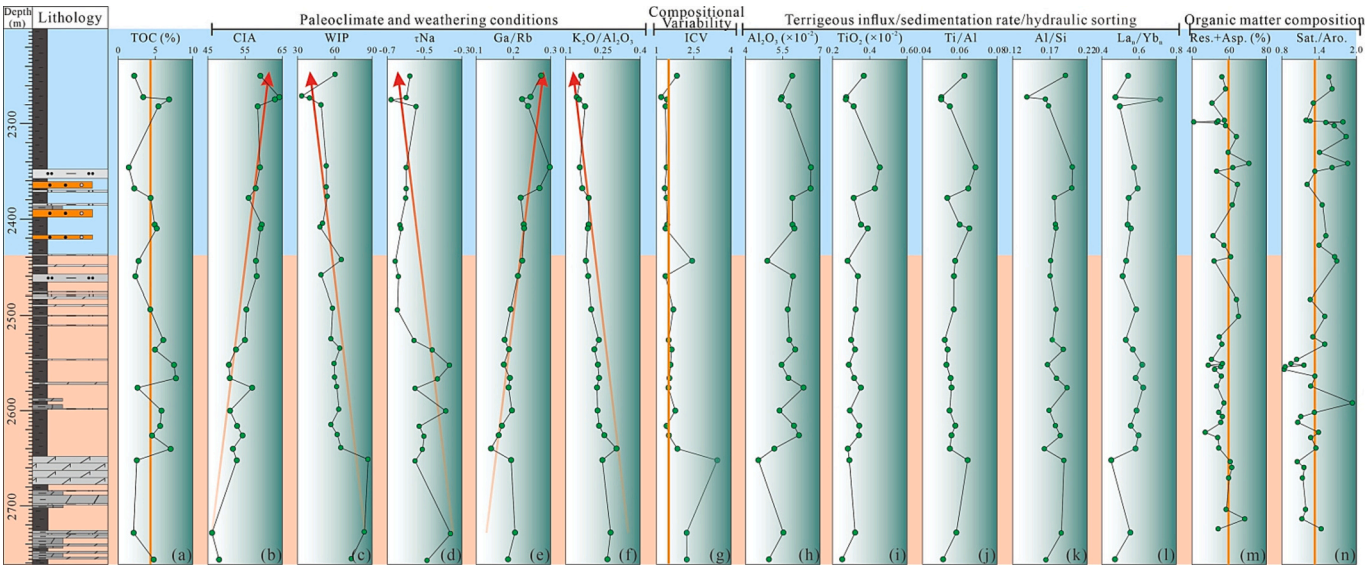

Fig. 14. Stratigraphic distributions of lithology, TOC content, extractable organic matter composition and geochemical indices related to paleoclimate, compositional variability, terrigenous influx, and paleosalinity.
Note: the data related to extractable organic matter composition was reported by Luo et al. (2018).

Fig. 15a also indicates the Mo/TOC ratios in the studied samples are lower than those in the Fort Worth Basin, which is similar to the case in the Pleistocene samples in the Qaidam Basin (Qiao et al., 2022). This anomaly might be caused by three reasons including high deposition rate, high water evaporation condition, and/or a lack of persistent and extensive H_2S-rich benthic water, which has been discussed by Qiao et al. (2022) in detail. Given the low deposition rate and cold/arid paleoclimate condition, the anomaly might be due to the lack of persistent and extensive H_2S-rich benthic water. The absence of a stable H_2S-rich reducing environment is reconfirmed by the rare pyrites and large size of framboidal pyrites (Fig. 5e, f, g and h). The low sulfur contents of the Lucaogou Formation were also inferred by Carroll (1998). The same result can be also affirmed by the plot of Mo_{EF} vs. U_{EF} co-variation (Fig. 15b). Fig. 15b shows relatively strong enrichments of Mo_{EF} as compared to U_{EF}, indicating the operation of a metal-oxyhydroxide particulate shuttle increases the export of Mo from aqueous to sediments but has little effect on aqueous U (Tribovillard et al., 2012). Moreover, the analyzed samples are located in the field of the weakest cycle 1 field representing suboxic conditions (Tribovillard et al., 2012). In this case, the paleoredox parameters related to U are unavailable based on the previous thresholds (Jones and Manning, 1994) due to the low concentrations of U. Moreover, based on the principle that the C_{org}/P ratio > 100 corresponds to reducing conditions but <50 indicates oxidizing environments (Algeo and Li, 2020), the C_{org}/P ratios for the studied samples ranging from 28.78 to 137.04 (73.91 on average) indicate suboxic benthic water conditions as well (Fig. 16f; Table 5). The surface waters were well-oxygenated, which can be demonstrated by the existence of Nestoria fossils (Fig. 2). Moreover, the rest common indicators, e.g., V/Cr, Ni/Co, and (V + Ni)/V, show similar trends to the U_{EF}, Mo_{EF} and C_{org}/P indicating they were affected by paleoredox conditions to some extent (Fig. 16d-i). However, these indicators' thresholds proposed by Jones and Manning (1994) are not suitable for the studied samples because there is no basis for calculating a paleoredox threshold for one formation (or set of formations) to be fully applicable to other formations of different ages and depositional settings (Algeo and Liu, 2020). In addition, there is no clear difference in these elemental indicators and biomarker parameters between the lower and upper members (e.g., DBT/PHE; Luo et al., 2018), indicating the stable benthic water paleoredox conditions experienced limited agitation of external water inflow in the upper member.

5.4. Paleoproductivity

Paleoproductivity may be one of the most important factors affecting the development of OM-rich sediments. Indicators, e.g., original organic carbon, Si_{bio}, and phosphorus (P) contents, as well as trace elements concentrations (e.g., Ni, Ba, Zn and Cu), can be used to evaluate paleoproductivity (Dymond et al., 1992; Tribovillard et al., 2006; Schoepfer et al., 2015; Shen et al., 2015; Arsairai et al., 2016). As mentioned above, terrestrial higher plants exerted little effect on the OM composition in the study area, so the paleoproductivity-related proxies are reliable.

Generally, Si_{bio} originated from siliceous organisms, e.g., diatoms, radiolarians, and sponge spicules, which can be used as an indicator of paleoproductivity (Wu et al., 2022). The Si_{bio} concentrations show a similar trend with the TOC contents (Fig. 16a and j) but reverse trends with both the Al_2O_3 and TiO_2 (Fig. 14h and I), indicating the Si_{bio} is a reliable indicator for the evaluation of paleoproductivity and terrigenous OM input was limited. The Si_{bio} values are 0.29–9.44 with an average value of 3.24, which indicates a moderate paleoproductivity (Fig. 16j and Table 1).

Nutrient elements, such as Cu and Ni, combine with OM or form organic complex compounds to deposit, and the remineralized Cu and Ni can be trapped by sedimentary pyrite during the OM decomposition (Piper and Perkins, 2004; Schoepfer et al., 2015), so they can be used to evaluate paleoproductivity. In general, Al is resistant to weathering and diagenesis, so its concentration represents clay minerals in fine-grained clastic sedimentary rocks/sediments (Calvert and Pedersen, 2007). Elements normalized to Al are regarded as the concentrations after eliminating the effect of debris input. Ni/Al and Cu/Al ratios are used as proxies of paleoproductivity in this study. As shown in Fig. 16m and n, both the Ni/Al and Cu/Al ratios are positively related to TOC contents in vertical distribution patterns. The Cu/Al ratios of 4.96–8.70 ppm/% and Ni/Al ratios of 4.93–10.28 ppm/% (Table 5) indicate a moderate paleoproductivity as compared to the Cu/Al (avg. 15.2 ppm/%) and Ni/Al (avg. 23.38 ppm/%) ratios in offshore Peru with high upwelling productivity (Böning et al., 2004).

As compared to the paleoproductivity evaluated above, the underestimation of paleoproductivity based on P and Ba is possible in this least-reducing situation, because P and Ba escape easily in reducing environments (Schoepfer et al., 2015). In Fig. 16k and l, both the P and Ba show different vertical distribution patterns from the above paleoproductivity indicators, indicating they are affected by paleoredox

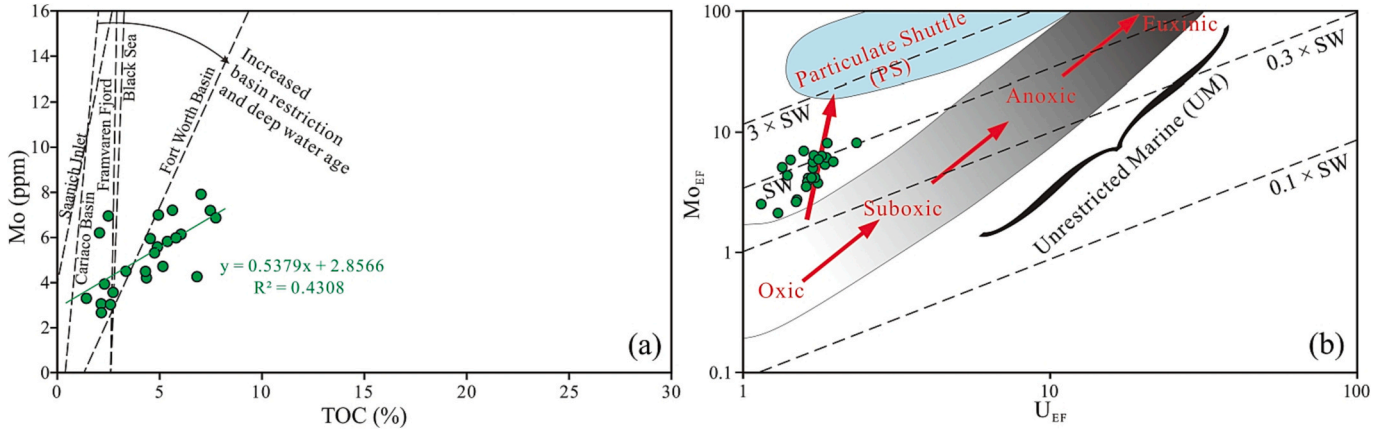

Fig. 15. (a) Comparison of TOC–Mo relationship among results of this study, Barnett Formation in the Fort Worth Basin and those of modern anoxic silled-basin environments (the TOC–Mo regression line slopes and previous studies data are given in Rowe et al. (2008) and (b) U_{EF} vs. Mo_{EF} (modified after Tribovillard et al., 2012).
Note: the TOC contents used in Rowe et al. (2008) are original TOC_o ($TOC_o = TOC_{meas}/(1–0.363)$, so the slope for the Fort Worth Basin should be a little bit steeper).

conditions to some extent. However, the Ba_{bio} of 0–2109 ppm (762 ppm on average) verifies the above evaluation. The moderate paleoproductivity is further corroborated by the P_{bio} (339–3305 ppm with 972 ppm on average; Table 5) which is an essential nutrient element in the metabolic activities of organisms (Dymond et al., 1992; Tribovillard et al., 2006; Schoepfer et al., 2015). The moderate paleoproductivity is consistent with the conclusion argued by Carroll (1998). In addition, the small variations of paleoproductivity proxies in the profile (Fig. 16j-n) indicate the small changes in paleoproductivity over time. Considering the wide distribution of tuffaceous shale in the Lucaogou Formation, volcanic activities/ash might be a major provider of nutrients to promote the breeding of the algae and cyanobacteria, as the Sinian source rocks in the Yangtze craton and the Triassic Chang 7 Member source rocks in the Ordos Basin are (Liu et al., 2019; Liu et al., 2021; Qiao et al., 2021b).

5.5. OM accumulation controlling factors

OM accumulation is a complex physical and chemical process, which is mainly controlled by primary productivity, benthic water redox condition, and/or deposition rate (Katz, 2001; Sageman et al., 2003; Pichevin et al., 2004; Mort et al., 2007).

Theoretically, detrital input has two effects on OM preservation (Ibach, 1982; Littke, 1993; Algeo et al., 2013). On the one hand, it is conducive to OM accumulation because the input of terrigenous OM, high deposition rates and calm waters are essential conditions for the well-preserved OM in oxygen-rich sub-aquatic environments (Pichevin et al., 2004; Qiao et al., 2021b). On the other hand, detrital input results in a dilution effect on OM accumulation (Qiao et al., 2021a). As discussed above, the flourish and supplement of terrigenous OM were limited due to the cold/arid paleoclimate, so it did not play a positive role. Moreover, there is no clear relationship between the TOC contents and each of the Ti/Al, Al/Si, and La_n/Yb_n ratios, indicating the low deposition rate had little effect on the OM accumulation for the studied samples (Fig. 14a, j-i). So, the main factors of OM accumulation for the studied samples might be the benthic water paleoredox conditions and/or the primary productivity.

Upwelling is an important supply of nutrients from deep water (Schoepfer et al., 2013). Sweere et al. (2016) used Mn and Co concentrations to recognize the upwelling process with Co × Mn values of <0.4 because these two elements are enriched in restricted basins due to slow deep-water renewal rates and fluvial inputs but depleted in upwelling

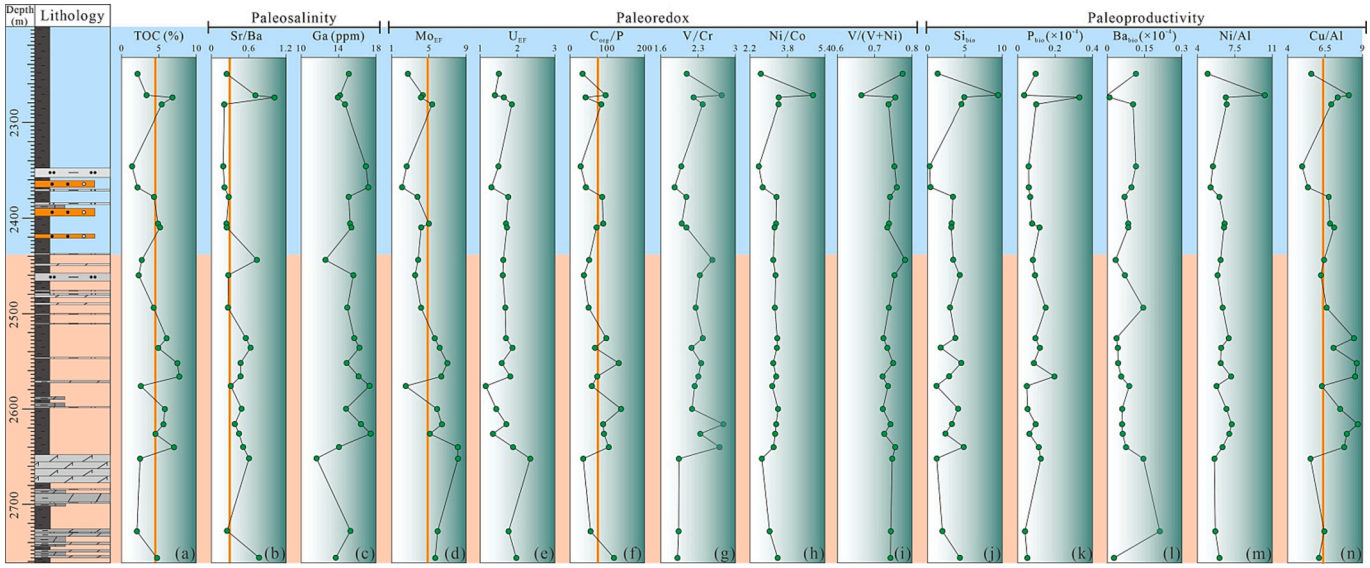

Fig. 16. Stratigraphic distributions of lithology, TOC content and geochemical indices related to paleoredox and paleoproductivity.

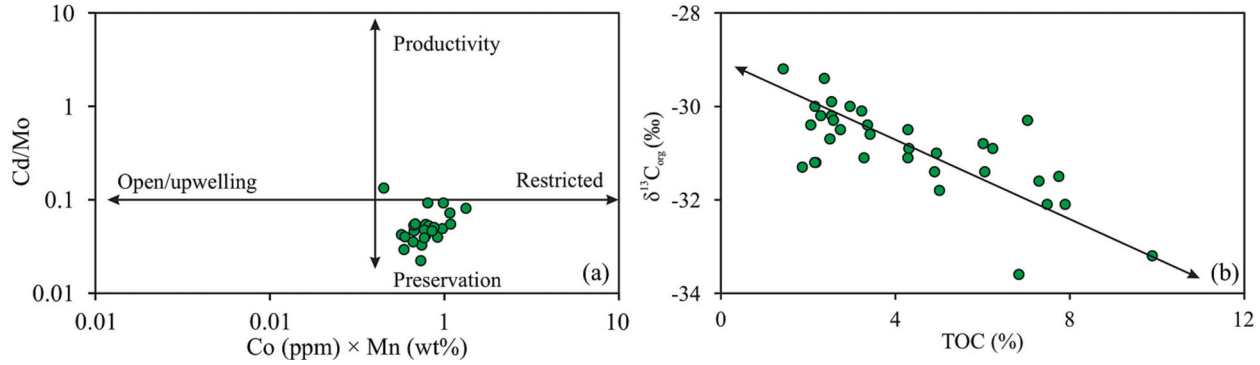

Fig. 17. Cross plots of (a) Co (ppm) × Mn (%) values vs. Cd/Mo ratios (after Sweere et al., 2016) and (b) TOC contents vs. stable carbon isotope compositions of organic matter, illustrating the controlling factors on OM accumulation.

environments. The Co × Mn values for the studied samples indicate the absence of upwelling in the paleolake, which is consistent with the result from Carroll (1998) who argued that the primary productivities were controlled by the limited nutrient supply dominated by volcanic rocks. Combined with the Cd/Mo ratios, Fig. 17a indicates that the preservation conditions (i.e., suboxic benthic waters and saline-hypersaline water columns) rather than the moderate paleoproductivity was the controlling factor for OM accumulation. The negative relationship between the TOC contents and stable carbon isotope compositions of OM also indicates that the paleoredox condition was more important (Fig. 17b) (Hollander and McKenzie, 1991; Freeman et al., 1990, 1994; Wachniew and Różański, 1997; Qiao et al., 2020, 2022). The ecosystem and preservation conditions also determined the low TOC contents in the study area. The TOC contents of the studied samples are slightly higher than the TOC contents in the lacustrine Qigequan Formation formed without the input of volcanic nutrients under cold and arid paleoclimate conditions in the Qaidam Basin (Qiao et al., 2021a), but far lower than those in the lacustrine Chang 7 Member with plenty of volcanic nutrients input under warm and humid paleoclimate conditions in the Ordos Basin (Qiao et al., 2021b).

6. Conclusions

The Lucaogou Formation is a set of excellent alkaline oil shale developed in the Junggar Basin, which can be divided into two members. The lower member develops more dolomite fine-grained sediments which almost disappear in the upper member. By analyzing the characteristics of major element oxides, trace and rare-earth elements as well as organic petrography, we draw the following conclusions:

(1) The provenance of the studied succession was mainly derived from the Middle-Late Permian intermediate-felsic volcanic rocks (e.g., granodiorite, andesite and dacite) of the Tianshan Mountains under a continental island arc paleotectonic setting without recycling sediments.
(2) The paleoclimate conditions were cold/arid with weak chemical weathering in an episode with a warming and/or enhanced continental weathering trend. The trend is more likely to be caused by the increase in atmospheric pCO_2. Besides, the brackish to hypersaline conditions were prevailing with the salinity being higher in the lower member in comparison to that in the upper member. By contrast, the OM composition and suboxic benthic waters were kept stable during the deposition of the Lucaogou Formation.
(3) The studied samples developed moderate paleoproductivity caused by predominately algae and bacteria which might be associated with volcanic nutrients. However, the development of terrestrial OM was limited due to the cold/arid paleoclimate conditions over time.
(4) The OM accumulation was mainly controlled by the preservation conditions caused by the suboxic benthic waters and brackish to hypersaline water columns rather than the moderate paleoproductivity and the limited detrital inputs/low deposition rates.

CRediT authorship contribution statement

Jinqi Qiao: Conceptualization, Methodology, Funding acquisition, Formal analysis, Data curation, Writing – original draft. **Qingyong Luo:** Conceptualization, Methodology, Supervision, Writing – review & editing. **Kuihua Zhang:** Resources. **Guanlong Zhang:** Resources. **Jincai Duan:** Methodology, Formal analysis. **Dandan Wang:** Investigation, Formal analysis. **Hongzhou Yu:** Resources. **Shengzhu Wang:** Resources. **Yansheng Qu:** Resources. **Ludmila Kopaevich:** Writing – review & editing.

Declaration of Competing Interest

In this paper, we confirm that all authors have no conflict of interest to declare.

Data availability

Data will be made available on request.

Acknowledgements

I would like to express my gratitude to all those who have helped me during the writing of this manuscript. Thank all the team members of this paper for their hard work and teamwork. The study was granted financial support by National Natural Science Foundation of China (No. 42122016) and Science Foundation of China University of Petroleum, Beijing (No. ZX20220074).

Appendix A. Supplementary data

Supplementary data to this article can be found online at https://doi.org/10.1016/j.coal.2023.104198.

References

Algeo, T.J., Li, C., 2020. Redox classification and calibration of redox thresholds in sedimentary systems. Geochim. Cosmochim. Acta 287 (15), 8–26.
Algeo, T.J., Liu, J.S., 2020. A re-assessment of elemental proxies for paleoredox analysis. Chem. Geol. 540, 119549.
Algeo, T.J., Henderson, C.M., Tong, J.N., Feng, Q.L., Yin, H.F., Tyson, R.V., 2013. Plankton and productivity during the Permiane Triassic boundary crisis: an analysis of organic carbon fluxes. Glob. Planet. Chang. 105, 52–67.
Allègre, C.J., Michard, G., 2012. Introduction to Geochemistry, vol. 10. Springer Science & Business Media, p. 69.

Allen, M.B., Sengör, A.M.C., Natalin, B.A., 1995. Junggar, Turfan, and Alakol basins as late Permian to? Early Triassic extensional structures in a sinistral shear zone in the Altaid orogenic collage. Central Asia. J. Geol. Soc. London 152 (2), 327–338.
Arsairai, B., Wannakomol, A., Feng, Q.L., Chonglakmani, C., 2016. Paleoproductivity and Paleoredox Condition of the Huai Hin Lat Formation in Northeastern Thailand. J. Earth Sci. 27 (3), 350–364.
Bertrand, P., Shimmield, G., Martinez, P., Grousset, F., Jorissen, F., Paterne, M., Pujol, C., Bouloubassi, I., Menard, P.B., Peypouquet, J.P., Beaufort, L., Sicre, M.A., Lallier Verges, E., Foster, J.M., Ternois, Y., 1996. The glacial ocean productivity hypothesis: the importance of regional temporal and spatial studies. Mar. Geol. 130 (1–2), 1–9.
Bhat, M.I., Ghosh, S.K., 2001. Geochemistry of the 2.51 Ga old Rampur group pelites, western Himalayas: implications for their provenance and weathering. Precambrian Res. 108 (1–2), 1–16.
Bhatia, M.R., 1983. Plate tectonics and geochemical composition of sandstones. J. Geol. 91 (6), 611–627.
Bhatia, M.R., Crook, K.A., 1986. Trace element characteristics of graywackes and tectonic setting discrimination of sedimentary basins. Contrib. Mineral. Petrol. 92 (2), 181–193.
Böning, P., Brumsack, H.J., Bottcher, M.E., Schnetger, B., Kriete, C., Kallmeyer, J., Borchers, S.L., 2004. Geochemistry of Peruvian near surface sediments. Geochim. Cosmochim. Acta 68 (21), 4429–4451.
Bouchez, J., Gaillardet, J., France-Lanord, C., Maurice, L., Dutra-Maia, P., 2011. Grain size control of river suspended sediment geochemistry: clues from Amazon River depth profiles. Geochem. Geophys. Geosyst. 12 (3), 1–24.
Breiter, K., Gardenová, N., Kanický, V., Vaculovič, T., 2013. Gallium and germanium geochemistry during magmatic frac- tionation and post-magmatic alteration in different types of granitoids: a case study from the Bohemian Massif (Czech Republic). Geol. Carpath. 64 (3), 171–180.
Briffa, K.R., Osborn, T.J., Schweingruber, F.H., 2004. Large-scale temperature inferences from tree rings: a review. Glob. Planet. Chang. 40 (1–2), 11–26.
Cai, M.T., Fang, X.M., Wu, F.L., Miao, Y.F., Appel, E., 2012. Pliocene–Pleistocene stepwise drying of Central Asia: evidence from paleomagnetism and sporopollen record of the deep borehole SG-3 in the western Qaidam Basin. NE Tibetan Plateau. Glob. Planet. Chang. 94–95, 72–81.
Calvert, S.E., Pedersen, T.F., 2007. Chapter fourteen elemental proxies for palaeoclimatic and palaeoceanographic variability in marine sediments: interpretation and application. Dev. Mar. Geol. 1, 567–644.
Cao, J., Zhang, Y.J., Hu, W.X., Yao, S.P., Wang, X.L., Zhang, Y.Q., Tang, Y., 2005. The Permian hybrid petroleum system in the northwest margin of the Junggar Basin, Northwest China. Mar. Pet. Geol. 22 (3), 331–349.
Cao, J., Xia, L.W., Wang, T.T., Zhi, D.M., Tang, Y., Li, W.W., 2020. An alkaline lake in the late Paleozoic Ice Age (LPIA): a review and new insights into paleoenvironment and petroleum geology. Earth-Sci. Rev. 202, 103091.
Caplan, M.L., Bustin, R.M., 1999. Palaeoceanographic controls on geochemical characteristics of organic-rich Exshaw mudrocks: role of enhanced primary production. Org. Geochem. 30 (2–3), 161–188.
Carroll, A.R., 1998. Upper Permian lacustrine organic facies evolution, southern Junggar Basin, NW China. Org. Geochem. 28 (11), 649–667.
Carroll, A.R., Wartes, M.A., 2003. Organic Carbon Burial by Large Permian Lakes, Northwest China. 370. Geological Society of America Special Paper, pp. 91–104.
Chen, Z.Y., Chen, Z.L., Zhang, W.G., 1997. Quaternary stratigraphy and trace-element indices of the Yangtze Delta, eastern China, with special reference to marine transgressions. Quat. Res. 47 (2), 181–191.
Cheng, D.W., Zhou, C.M., Zhang, Z.J., Yuan, X.J., Liu, Y.H., Chen, X.Y., 2022. Paleo-Environment Reconstruction of the Middle Permian Lucaogou Formation, Southeastern Junggar Basin, NW China: Implications for the Mechanism of Organic Matter Enrichment in Ancient Lake. J. Earth Sci. 33 (4), 963–976.
Condie, K.C., 1993. Chemical composition and evolution of the upper continental crust: Contrasting results from surface samples and shales. Chem. Geol. 104 (1–4), 1–37.
Condie, K.C., Wronkiewicz, D.J., 1990. The Cr/Th ratio in Precambrian pelites from the Kaapvaal Craton as an index of craton evolution. Earth Planet. Sci. Lett. 97 (3–4), 256–267.
Cox, R., Lowe, D.R., Cullers, R.L., 1995. The influence of sediment recycling and basement composition on evolution of mudrock chemistry in the southwestern United States. Geochim. Cosmochim. Acta 59 (14), 2919–2940.
Cullers, R.L., 1995. The controls on the major-element and trace-element evolution of shales, siltstones and sandstones of Ordovician to Tertiary age in the Wet Mountains Region, Colorado, USA. Chem. Geol. 123 (1–4), 107–131.
Cullers, R.L., 2002. Implications of elemental concentrations for provenance, redox conditions, and metamorphic studies of shales and limestones near Pueblo, CO, USA. Chem. Geol. 191 (4), 305–327.
Cullers, R.L., Berendsen, P., 1998. The provenance and chemical variation of sandstones associated with the Mid-continent Rift System, USA. Eur. J. Mineral. 10 (5), 987–1002.
Cullers, R.L., Barrett, T., Carlson, R., Robinson, B., 1987. Rare-earth element and mineralogic changes in Holocene soil and stream sediment: a case study in the Wet Mountains, Colorado, USA. Chem. Geol. 63 (3–4), 275–297.
Dai, S., Wang, X., Zhou, Y., Hower, J.C., Li, D., Chen, W., Zhu, X., Zou, J., 2011. Chemical and mineralogical compositions of silicic, mafic, and alkali tonsteins in the late Permian coals from the Songzao Coalfield, Chongqing, Southwest China. Chem. Geol. 282, 29–44.
Dai, S., Zhang, W., Ward, C., Seredin, V.V., Hower, J.C., Li, X., Song, W., Wang, X., Kang, H., Zheng, L., Wang, P., Zhou, D., 2013. Mineralogical and geochemical anomalies of late Permian coals from the Fusui Coalfield, Guangxi Province, southern China: influences of terrigenous materials and hydrothermal fluids. Int. J. Coal Geol. 105, 60–84.
Dai, S., Li, T., Seredin, V.V., Ward, C.R., Hower, J.C., Zhou, Y., Zhang, M., Song, X., Song, W., Zhao, C., 2014. Origin of minerals and elements in the late Permian coals, tonsteins, and host rocks of the Xinde Mine, Xuanwei, eastern Yunnan, China. Int. J. Coal Geol. 121, 53–78.
Dai, S., Graham, I.T., Ward, C.R., 2016. A review of anomalous rare earth elements and yttrium in coal. Int. J. Coal Geol. 159, 82–95.
Dai, S., Ji, D., Ward, C.R., French, D., Hower, J.C., Yan, X., Wei, Q., 2018. Mississippian anthracites in Guangxi Province, southern China: petrological, mineralogical, and rare earth element evidence for high-temperature solutions. Int. J. Coal Geol. 197, 84–114.
Demaison, G., Huizinga, B.J., 1991. Genetic classification of petroleum systems. AAPG Bull. 75, 1626–1643.
Deng, T., Wang, X.M., Fortelius, M., Li, Q., Wang, Y., Tseng, Z.J.J., Takeuchi, G.T., Saylor, J.E., Säilä, L.K., Xie, G.P., 2011. Out of Tibet: Pliocene woolly rhino suggests high-plateau origin of Ice Age megaherbivores. Science. 333 (6047), 1285–1288.
Deng, K., Yang, S., Guo, Y., 2022. A global temperature control of silicate weathering intensity. Nat. Commun. 13 (1), 1781.
Dera, G., Pellenard, P., Neige, P., Deconinck, J.F., Pucéat, E., Dommergues, J.L., 2009. Distribution of clay minerals in early Jurassic Peritethyan seas: palaeoclimatic significance inferred from multiproxy comparisons. Palaeogeogr. Palaeoclimatol. Palaeoecol. 271 (1–2), 39–51.
Dymond, J., Suess, E., Lyle, M., 1992. Barium in deep-sea sediment: a geochemical proxy for paleoproductivity. Paleoceanogr. 7 (2), 163–181.
Fedo, C.M., Wayne Nesbitt, H., Young, G.M., 1995. Unraveling the effects of potassium metasomatism in sedimentary rocks and paleosols, with implications for paleoweathering conditions and provenance. Geology 23 (10), 921–924.
Feng, R., Kerrich, R., 1990. Geochemistry of fine-grained clastic sediments in the Archean Abitibi greenstone belt, Canada: implications for provenance and tectonic setting. Geochim. Cosmochim. Acta 54 (4), 1061–1081.
Fielding, C.R., Frank, T.D., Birgenheier, L.P., Rygel, M.C., Jones, A.T., Roberts, J., 2008a. Stratigraphic imprint of the late Paleozoic Ice Age in eastern Australia: a record of alternating glacial and nonglacial climate regime. Geol. Soc. London J. 165, 129–140.
Fielding, C.R., Frank, T.D., Birgenheier, L.P., Rygel, M.C., Jones, A.T., Roberts, J., 2008b. Stratigraphic record and facies associations of the late Paleozoic ice age in eastern Australia (New South Wales and Queensland). In: Fielding, C.R., Frank, T.D., Isbell, J.L. (Eds.), Resolving the Late Paleozoic Ice Age in Time and Space: Geological Society of America Special Paper, 441, pp. 41–58.
Fischer, H., Wahlen, M., Smith, J., Mastroianni, D., Deck, B., 1999. Ice core records of atmospheric CO2 around the last three glacial terminations. Science. 283 (5408), 1712–1714.
Fishman, N.S., Hackley, P.C., Lowers, H.A., Hill, R.J., Egenhoff, S.O., Eberl, D.D., Blume, A.E., 2012. The nature of porosity in organic-rich mudstones of the Upper Jurassic Kimmeridge Clay Formation, North Sea, offshore United Kingdom. Int. J. Coal Geol. 103, 32–50.
Floyd, P.A., Leveridge, B.E., 1987. Tectonic environment of the Devonian Gramscatho basin, South Cornwall: framework mode and geochemical evidence from turbiditic sandstones. J. Geol. Soc. 144, 531–542.
Freeman, K.H., Hayes, J.M., Trendel, J.M., Albrecht, P., 1990. Evidence from carbon isotope measurements for diverse origins of sedimentary hydrocarbons. Nature. 343 (6255), 254–256.
Freeman, K.H., Wakeham, S.G., Hayes, J.M., 1994. Predictive isotopic biogeochemistry: hydrocarbons from anoxic marine basins. Org. Geochem. 21 (6–7), 629–644.
Galy, V., France-Lanord, C., Lartiges, B., 2008. Loading and fate of particulate organic carbon from the Himalaya to the Ganga-Brahmaputra delta. Geochim. Cosmochim. Acta 72 (7), 1767–1787.
Garzanti, E., Ando, S., France-Lanord, C., Vezzoli, G., Censi, P., Galy, V., Najman, Y., 2010. Mineralogical and chemical variability of fluvial sediments 1. Bedload sand (Ganga– Brahmaputra, Bangladesh). Earth Planet. Sci. Lett. 299 (3–4), 368–381.
Garzanti, E., Ando, S., France-Lanord, C., Censi, P., Vignola, P., Galy, V., Lupker, M., 2011. Mineralogical and chemical variability of fluvial sediments 2. Suspended-load silt (Ganga– Brahmaputra, Bangladesh). Earth Planet. Sci. Lett. 302 (1–2), 107–120.
Garzanti, E., Padoan, M., Peruta, L., Setti, M., Najman, Y., Villa, I.M., 2013. Weathering geochemistry and Sr–Nd fingerprints of equatorial upper Nile and Congo muds. Geochem. Geophys. Geosyst. 14 (2), 292–316.
Gehrels, G., 2014. Detrital zircon U-Pb geochronology applied to tectonics. Annu. Rev. Earth Planet. Sci. 42, 127–149.
Gernon, T.M., Hincks, T.K., Merdith, A.S., Rohling, E.J., Palmer, M.R., Foster, G.L., Bataille, C.P., Müller, R.D., 2021. Global chemical weathering dominated by continental arcs since the mid-Palaeozoic. Nat. Geosci. 14 (9), 690–696.
Greber, N.D., Dauphas, N., 2019. The chemistry of fine-grained terrigenous sediments reveals a chemically evolved Paleoarchean emerged crust. Geochim. Cosmochim. Acta 255, 247–264.
Guo, Y.L., Yang, S.Y., Su, N., Li, C., Yin, P., Wang, Z.B., 2018. Revisiting the effects of hydrodynamic sorting and sedimentary recycling on chemical weathering indices. Geochim. Cosmochim. Acta 227, 48–63.
Hackley, P.C., Fishman, N., Wu, T., Baugher, G., 2016. Organic petrology and geochemistry of mudrocks from the lacustrine Lucaogou Formation, Santanghu Basin, Northwest China: application to lake basin evolution. Int. J. Coal Geol. 168, 20–34.
Helz, G.R., Miller, C.V., Charnock, J.M., Mosselmans, J.F.W., Pattrick, R.A.D., Garner, C. D., Vaughan, D.J., 1996. Mechanism of molybdenum removal from the sea and its concentration in black shales: EXAFS evidence. Geochim. Cosmochim. Acta 60 (19), 3631–3642.
Herron, M.M., 1988. Geochemical classification of terrigenous sands and shales from core or log data. J. Sediment. Res. 58 (5), 820–829.

Hollander, D.J., McKenzie, J.A., 1991. CO2 control on carbon-isotope fractionation during aqueous photosynthesis: a paleo-pCO2 barometer. Geology. 19 (9), 929–932.
Hou, M.G., Zha, M., Ding, X.J., Yin, H., Bian, B.L., Liu, H.L., Jiang, Z.F., 2021. Source and accumulation process of jurassic biodegraded oil in the eastern junggar basin, NW China. Pet. Sci. 18 (4), 1033–1046.
Huang, H., Gao, Y., Jones, M.M., Tao, H.F., Carroll, A.R., Ibarra, D.E., Wu, H.C., Wang, C. S., 2020. Astronomical forcing of middle permian terrestrial climate recorded in a large paleolake in northwestern China. Palaeogeogr. Palaeoclimatol. Palaeoecol. 550, 109735.
Ibach, L.E.J., 1982. Relationship between sedimentation rate and total organic carbon content in ancient marine sediments. AAPG Bull. 66 (2), 170–188.
ICCP, 1998. The new vitrinite classification (ICCP System 1994). Fuel 77, 349–358.
ICCP, 2001. The new inertinite classification (ICCP System 1994). Fuel 80, 459–471.
Jarvie, D.M., 2012. Shale resource systems for oil and gas: part 2—Shale-oil resource systems. AAPG Spe. Vol. 89–119.
Jarvie, D.M., Hill, R.J., Ruble, T.E., Pollastro, R.M., 2007. Unconventional shale-gas systems: the Mississippian Barnett Shale of north-Central Texas as one model for thermogenic shale-gas assessment. AAPG Bull. 91 (4), 475–499.
Jian, X., Guan, P., Zhang, W., Feng, F., 2013. Geochemistry of Mesozoic and Cenozoic sediments in the northern Qaidam basin, northeastern Tibetan Plateau: implications for provenance and weathering. Chem. Geol. 360, 74–88.
Jones, B., Manning, D.A.C., 1994. Comparison of geochemical indices used for the interpretation of palaeoredox conditions in ancient mudstones. Chem. Geol. 111 (1–4), 111–129.
Katz, B.J., 2001. Lacustrine basin hydrocarbon exploration-current thoughts. J. Paleolimnol. 26, 161–179.
Kemp, S.J., Ellis, M.A., Mounteney, I., Kender, S., 2016. Palaeoclimatic implications of high-resolution clay mineral assemblages preceding and across the onset of the Palaeocene–Eocene Thermal Maximum, North Sea Basin. Clay Miner. 51 (5), 793–813.
Laceby, J.P., Evrard, O., Smith, H.G., Blake, W.H., Olley, J.M., Minella, J.P.G., Owens, P. N., 2017. The challenges and opportunities of addressing particle size effects in sediment source fingerprinting: a review. Earth-Sci. Rev. 169, 85–103.
LaMaskin, T.A., Dorsey, R.J., Vervoort, J.D., 2008. Tectonic controls on mudrock geochemistry, Mesozoic rocks of eastern Oregon and western Idaho, USA: implications for Cordilleran tectonics. J. Sediment. Res. 78 (12), 765–783.
Littke, R., 1993. Deposition of organic matter-rich sediments. In: Deposition, Diagenesis and Weathering of Organic Matter-Rich Sediments, pp. 12–45.
Liu, Q.Y., Zhu, D.Y., Jin, Z.J., Meng, Q.Q., Li, S.J., 2019. Influence of volcanic activities on redox chemistry changes linked to the enhancement of the ancient Sinian source rocks in the Yangtze craton. Precambrian Res. 327, 1–13.
Liu, Q., Li, P., Jin, Z., Liang, X., Zhu, D., Wu, X., Meng, Q., Liu, J., Fu, Q., Zhao, J., 2021. Preservation of organic matter in shale linked to bacterial sulfate reduction (BSR) and volcanic activity under marine and lacustrine depositional environments. Mar. Pet. Geol. 127, 104950.
Lowry, D.P., Poulsen, C.J., Horton, D.E., Torsvik, T.H., Pollard, D., 2014. Thresholds for Paleozoic ice sheet initiation. Geology. 42 (7), 627–630.
Luo, Q.Y., George, S.C., Xu, Y.H., Zhong, N.N., 2016. Organic geochemical characteristics of the Mesoproterozoic Hongshuizhuang Formation from northern China: implications for thermal maturity and biological sources. Org. Geochem. 99, 23–37.
Luo, Q.Y., Gong, L., Qu, Y.S., Zhang, K.H., Zhang, G.L., Wang, S.Z., 2018. The tight oil potential of the lucaogou formation from the southern Junggar basin, China. Fuel. 234, 858–871.
Lupker, M., France-Lanord, C., Galy, V., Lave, J., Gaillardet, J., Gajurel, A.P., Guilmette, C., Rahman, M., Singh, S.K., Sinha, R., 2012. Predominant floodplain over mountain weathering of Himalayan sediments (Ganga basin). Geochim. Cosmochim. Acta 84, 410–432.
Ma, J., Huang, Z., Gao, X., Chen, C., 2015. Oil–source rock correlation for tight oil in tuffaceous reservoirs in the Permian Tiaohu Formation, Santanghu Basin, Northwest China. Can. J. Earth Sci. 52 (11), 1014–1026.
Malengreau, N., Muller, J.P., Calas, G., 1995. Spectroscopic approach for investigating the status and mobility of Ti in kaolinitic materials. Clay Clay Miner. 43, 615–621.
McCulloch, M.T., Wasserburg, G.J., 1978. Sm-nd and rb-sr chronology of continental crust formation. Science 200 (4345), 1003–1011.
McLennan, S.M., 1989. Rare earth elements in sedimentary rocks: influence of provenance and sedimentary process. In: Lipin, B.R., McKay, G.A. (Eds.), Geochemistry and Mineralogy of Rare Earth Elements: Reviews in Mineralogy, 21, pp. 169–200.
Mclennan, S.M., 1993. Weathering and global denudation. J. Geol. 101 (2), 295–303.
McLennan, S.M., 2001. Relationships between the trace element composition of sedimentary rocks and upper continental crust. Geochem. Geophys. Geosyst. 2, 2000GC000109.
McLennan, S.M., Taylor, S.R., 1991. Sedimentary rocks and crustal evolution: tectonic setting and secular trends. J. Geol. 99 (1), 1–21.
McLennan, S.M., Taylor, S.R., McCulloch, M.T., Maynard, J.B., 1990. Geochemical and Nd-Sr isotopic composition of deep-sea turbidites: crustal evolution and plate tectonic associations. Geochim. Cosmochim. Acta 54 (7), 2015–2050.
McLennan, S.M., Hemming, S., McDaniel, D.K., Hanson, G.N., 1993. Geochemical approaches to sedimentation, provenance, and tectonics. Spe. Papers-Geol. Soc. America 21–40.
Meunier, A., Caner, L., Hubert, F., El Albani, A., Pret, D., 2013. The Weathering Intensity Scale (WIS): an alternative approach of the chemical index of alteration (CIA). Am. J. Sci. 313 (2), 113–143.
Meyers, P.A., 1997. Organic geochemical proxies of paleoceanographic, paleolimnologic, and paleoclimatic processes. Org. Geochem. 27 (5–6), 213–250.
Mongelli, G., Critelli, S., Perri, F., Sonnino, M., Perrone, V., 2006. Sedimentary recycling, provenance and paleo-weathering from chemistry and mineralogy of Mesozoic continental redbed mudrocks, Peloritani mountains. Southern Italy. Geochem. J. 40 (2), 197–209.
Mort, H., Jacquat, O., Adatte, T., Steinmann, P., Föllmi, K., Matera, V., Berner, Z., Stüben, D., 2007. The Cenomanian/Turonian anoxic event at the Bonarelli Level in Italy and Spain: enhanced productivity and/or better preservation? Cretac. Res. 28 (4), 597–612.
Murphy, A.E., Sageman, B.B., Hollander, D.J., Lyons, T.W., Brett, C.E., 2000. Black shale, deposition and faunal overturn in the Devonian Appalachian Basin: clastic starvation, seasonal water-column mixing, and efficient biolimiting nutrient recycling. Paleoceanogr. 15 (3), 280–291.
Nesbitt, H.W., Young, G.M., 1982. Early Proterozoic climates and plate motions inferred from major element chemistry of lutites. Nature. 299 (5885), 715–717.
Nesbitt, H.W., Young, G.M., 1984. Prediction of some weathering trends of plutonic and volcanic rocks based on thermodynamic and kinetic considerations. Geochim. Cosmochim. Acta 48 (7), 1523–1534.
Ohta, T., Arai, H., 2007. Statistical empirical index of chemical weathering in igneous rocks: a new tool for evaluating the degree of weathering. Chem. Geol. 240 (3–4), 280–297.
Parker, A., 1970. An index of weathering for silicate rocks. Geol. Mag. 107 (6), 501–504.
Peters, K.E., Walters, C.C., Moldowan, J.M., 2005. The Biomarker Guide: Volume II Biomarkers and Isotopes in Petroleum Exploration and Earth History. Cambridge University Press, United Kingdom, pp. 483–487.
Pichevin, L., Bertrand, P., Boussafr, M., Disnar, J.R., 2004. Organic matter accumulation and preservation controls in a deep-sea modern environment: an example from Namibian slope sediments. Org. Geochem. 35, 543–559.
Pickel, W., Kus, J., Flores, D., Kalaitzidis, S., Christanis, K., Cardott, B.J., MiszKennan, M., Rodrigues, S., Hentschel, A., Hamor-Vido, M., Crosdale, P., Wagner, N., ICCP, 2017. Classification of liptinite – ICCP System 1994. Int. J. Coal Geol. 169, 40–61.
Piper, D.Z., Perkins, R.B., 2004. A modern vs. Permian black shale—the hydrography, primary productivity, and water-column chemistry of deposition. Chem. Geol. 206 (3–4), 177–197.
Potter, P.E., Maynard, J.B., Depetris, P.J., 2005. Mud and mudstones: Introduction and overview. Springer Science & Business Media. J. Sediment. Res. 56 (3), 329–345.
Qiao, J., Liu, L.F., Shang, X.Q., 2020. Deposition conditions of the jurassic lacustrine source rocks in the East Fukang sag, junggar basin, nw China: evidence from major and trace elements. Geol. J. 55 (7), 4936–4953.
Qiao, J., Grohmann, S., Baniasad, A., Zhang, C., Jiang, Z.X., Littke, R., 2021a. High microbial gas potential of Pleistocene lacustrine deposits in the central Qaidam Basin, China: an organic geochemical and petrographic assessment. Int. J. Coal Geol. 245, 103818.
Qiao, J., Baniasad, A., Zieger, L., Zhang, C., Luo, Q., Littke, R., 2021b. Paleo-depositional environment, origin and characteristics of organic matter of the Triassic Chang 7 Member of the Yanchang Formation throughout the mid-western part of the Ordos Basin, China. Int. J. Coal Geol. 237, 103636.
Qiao, J., Littke, R., Grohmann, S., Zhang, C., Jiang, Z.X., Strauss, H., Zieger, L., 2022. Climatic and environmental conditions during the Pleistocene in the Central Qaidam Basin, NE Tibetan Plateau: evidence from GDGTs, stable isotopes and major and trace elements of the Qigequan Formation. Int. J. Coal Geol. 254, 103958.
Qiao, J., Luo, Q., Zhang, Y., Wang, D., Cui, H., Shang, X., Liu, L., Zhang, T., 2023. Formation conditions and enrichment mechanisms of the Jurassic lacustrine organic-rich shale in the East Fukang Sag, Junggar Basin, NW China: a reassessment based on organic geochemistry. Front. Earth Sci. 11, 1086827.
Qie, W., Algeo, T.J., Luo, G., Herrmann, A., 2019. Global events of the late paleozoic (early devonian to middle permian): a review. Palaeogeogr. Palaeoclimatol. Palaeoecol. 531, 109259.
Rasmussen, C., Brantley, S., Richter, D.D., Blum, A., Dixon, J., White, A.F., 2011. Strong climate and tectonic control on plagioclase weathering in granitic terrain. Earth Planet. Sci. Lett. 301, 521–530.
Romero-Viana, L., Kienel, U., Sachse, D., 2012. Lipid biomarker signatures in a hypersaline lake on Isabel Island (Eastern Pacifc) as a proxy for past rainfall anomaly (1942–2006 AD). Palaeogeogr. Palaeoclimatol. Palaeoecol. 350–352, 49–61.
Roser, B.P., Korsch, R.J., 1986. Determination of tectonic setting of sandstone-mudstone suites using SiO2 content and K2O/Na2O ratio. J. Geol. 94 (5), 635–650.
Ross, D.J.K., Bustin, R.M., 2009. Investigating the use of sedimentary geochemical proxies for paleoenvironment interpretation of thermally mature organic-rich strata: examples from the Devonian–Mississippian shales, Western Canadian Sedimentary Basin. Chem. Geol. 260 (1–2), 1–19.
Rowe, H.D., Loucks, R.G., Ruppel, S.C., Rimmer, S.M., 2008. Mississippian Barnett Formation, Fort Worth Basin, Texas: Bulk geochemical inferences and Mo–TOC constraints on the severity of hydrographic restriction. Chem. Geol. 257 (1–2), 16–25.
Roy, D.K., Roser, B.P., 2013. Climatic control on the composition of Carboniferous–Permian Gondwana sediments, Khalaspir basin, Bangladesh. Gondwana Res. 23 (3), 1163–1171.
Ryan, K.M., Williams, D.M., 2007. Testing the reliability of discrimination diagrams for determining the tectonic depositional environment of ancient sedimentary basins. Chem. Geol. 242 (1–2), 103–125.
Sageman, B.B., Murphy, A.E., Werne, J.P., Ver Straeten, C.A., Hollander, D.J., Lyons, T. W., 2003. A tale of shales: the relative roles of production, decomposition, and dilution in the accumulation of organic-rich strata, Middle-Upper Devonian, appalachian basin. Chem. Geol. 195 (1–4), 229–273.

Salminen, R., Batista, M.J., Bidovec, M., Demetriades, A., De Vivo, B., De Vos, W., 2005. FOREGS Geochemical Atlas of Europe, Part I: Background Information, Methodology, and Maps. Geological Survey of Finland, Espoo.
Sawant, S.S., Kumar, K.V., Balaram, V., Rao, D.S., Rao, K.S., Tiwari, R.P., 2017. Geochemistry and genesis of craton-derived sediments from active continental margins: insights from the Mizoram foreland basin, NE India. Chem. Geol. 40 (20), 13–32.
Schoepfer, S.D., Henderson, C.M., Garrison, G.H., Foriel, J., Ward, P.D., Selby, D., Hower, J.C., Algeo, T.J., Shen, Y.N., 2013. Termination of a continent–margin upwelling system at the permian–triassic boundary (opal creek, Alberta, Canada). Glob. Planet. Chang. 105, 21–35.
Schoepfer, S.D., Shen, J., Wei, H.Y., Tyson, R.V., Ingall, E., Algeo, T.J., 2015. Total organic carbon, organic phosphorus, and biogenic barium fluxes as proxies for paleomarine productivity. Earth-Sci. Rev. 149, 23–52.
Shen, J., Schoepfer, S.D., Feng, Q.L., Zhou, L., Yu, J.X., Song, H.Y., Wei, H.Y., Algeo, T.J., 2015. Marine productivity changes during the end-Permian crisis and early Triassic recovery. Earth-Sci. Rev. 149, 136–162.
Song, Y.G., Wang, Q.S., An, Z.S., Qiang, X.K., Dong, J.B., Chang, H., Zhang, M.S., Guo, X. H., 2018. Mid-Miocene climatic optimum: Clay mineral evidence from the red clay succession, Longzhong Basin, Northern China. Palaeogeogr. Palaeoclimatol. Palaeoecol. 512, 46–55.
Sun, F., Hu, W., Cao, J., Wang, X., Zhang, Z., Ramezani, J., Shen, S., 2022. Sustained and intensified lacustrine methane cycling during early Permian climate warming. Nat. Commun. 13, 4856.
Suttner, L.J., Dutta, P.K., 1986. Alluvial sandstone composition and paleoclimate; I, framework mineralogy. J. Sediment. Res. 56 (3), 329–345.
Svensson, A., Andersen, K.K., Bigler, M., Clausen, H.B., Dahl-Jensen, D., Davies, S.M., Johnsen, S.J., Muscheler, Ra, Rasmussen, S.O., Röthlisberger, R., Steffensen, J.P., Vinther, B.M., 2006. The Greenland ice core chronology 2005, 15–42 ka. Part 2: comparison to other records. Quat. Sci. Rev. 25 (23–24), 3258–3267.
Sweere, T., van den Boorn, S., Dickson, A.J., Reichart, G.J., 2016. Definition of new trace metal proxies for the controls on organic matter enrichment in marine sediments based on Mn, Co, Mo and Cd concentrations. Chem. Geol. 441, 235–245.
Tang, W.H., Zhang, Z.C., Li, J.F., Li, K., Chen, Y., Guo, Z.J., 2014. Late Paleozoic to Jurassic tectonic evolution of the Bogda area (Northwest China): evidence from detrital zircon U-Pb geochronology. Tectonophysics 626, 144–156.
Tang, Y., Cao, J., He, W.J., Guo, X.G., Zhao, K.B., Li, W.W., 2021. Discovery of shale oil in alkaline lacustrine basins: the late paleozoic Fengcheng formation, Mahu sag, Junggar Basin, China. Pet. Sci. 18 (5), 1281–1293.
Tao, S., Xu, Y., Tang, D., Xu, H., Li, S., Chen, S., Liu, W., Cui, Y., Guo, M., 2017. Geochemistry of the shitoumei oil shale in the Santanghu basin, Northwest China: implications for paleoclimate conditions, weathering, provenance and tectonic setting. Int. J. Coal Geol. 184, 42–56.
Taylor, S.R., McLennan, S.M., 1985. The Continental Crust: Its Composition and Evolution. Blackwell, Oxford, p. 312.
Tian, H., Li, T.F., Zhang, T.W., Xiao, X.M., 2016. Characterization of methane adsorption on overmature Lower Silurian–Upper Ordovician shales in Sichuan Basin, southwest China: experimental results and geological implications. Int. J. Coal Geol. 156, 36–49.
Tribovillard, N., Algeo, T.J., Lyons, T., Riboulleau, A., 2006. Trace metals as paleoredox and paleoproductivity proxies: an update. Chem. Geol. 232 (1–2), 12–32.
Tribovillard, N., Algeo, T.J., Baudin, F., Riboulleau, A., 2012. Analysis of marine environmental conditions based on molybdenum–uranium covariation—applications to Mesozoic paleoceanography. Chem. Geol. 324, 46–58.
Wachniew, P., Różański, K., 1997. Carbon budget of a mid-latitude, groundwater-controlled lake: isotopic evidence for the importance of dissolved inorganic carbon recycling. Geochim. Cosmochim. Acta 61 (12), 2453–2465.
Wang, J.L., Wu, C.D., Li, Z., Zhu, W., Zhou, T.Q., Wu, J., Wang, J., 2018. The tectonic evolution of the Bogda region from Late Carboniferous to Triassic time: evidence from detrital zircon U–Pb geochronology and sandstone petrography. Geol. Mag. 155, 1063–1088.
Wang, T.T., Cao, J., Xia, L.W., Zhi, D.M., Tang, Y., He, W.J., 2022. Revised age of the Fengcheng formation, junggar basin, China: global implications for the late paleozoic ice age. Glob. Planet. Chang. 208, 103725.
Wartes, M.A., Carroll, A.R., Greene, T.J., 2002. Permian stratigraphic evolution of the Turpan-Hami Basin and adjacent regions, Northwest China: Constraints on post-amalgamation tectonic evolution. Geol. Soc. Am. Bull. 114, 131–152.
Wei, W., Algeo, T.J., 2020. Elemental proxies for paleosalinity analysis of ancient shales and mudrocks. Geochim. Cosmochim. Acta 287, 341–366.
Winchester, J.A., Floyd, P.A., 1977. Geochemical discrimination of different magma series and their differentiation products using immobile elements. Chem. Geol. 20, 325–343.
Wu, Z.R., He, S., He, Z.L., Li, X.C., Zhai, G.Y., Huang, Z.Q., 2022. Petrographical and geochemical characterization of the Upper Permian Longtan formation and Dalong Formation in the lower Yangtze region, South China: implications for provenance, paleoclimate, paleoenvironment and organic matter accumulation mechanisms. Mar. Pet. Geol. 139, 105580.
Yan, X., Dai, S., Graham, I.T., He, X., Shan, K., Liu, X., 2018. Determination of Eu concentrations in coal, fly ash and sedimentary rocks using a cation exchange resin and inductively coupled plasma mass spectrometry (ICP-MS). Int. J. Coal Geol. 191, 152–156.
Yang, W., Feng, Q., Liu, Y., Tabor, N., Miggins, D., Crowley, J.L., Lin, J., Thomas, S., 2010. Depositional environments and cyclo- and chronostratigraphy of uppermost Carboniferous–Lower Triassic fluvial–lacustrine deposits, southern Bogda Mountains, NW China—a terrestrial paleoclimatic record of mid-latitude NE Pangea. Glob. Planet. Chang. 73, 15–113.
Yang, W., Jolivet, M., Dupont-Nivet, G., Guo, Z.J., Zhang, Z.C., Wu, C.D., 2013. Source to sink relations between the Tian Shan and Junggar Basin (Northwest China) from late Palaeozoic to Quaternary: evidence from detrital U-Pb zircon geochronology. Basin Res. 25 (2), 219–240.
Zhang, H.R., Torsvik, T.H., 2022. Circum-Tethyan magmatic provinces, shifting continents and Permian climate change. Earth Planet. Sci. Lett. 584, 117453.
Zhang, M., Liu, Z., Xu, S., Sun, P., Hu, X., 2013. Element response to the Ancient lake information and its evolution history of argillaceous source rocks in the lucaogou formation in sangonghe area of Southern margin of Junggar Basin. J. Earth Sci. 24 (6), 987–996.
Zhao, M.Y., Zheng, Y.F., 2015. The intensity of chemical weathering: geochemical constraints from marine detrital sediments of Triassic age in South China. Chem. Geol. 391, 111–122.
Zhao, R., Zhang, J.Y., Zhou, C.M., Zhang, Z.J., Chen, S., Stockli, D.F., Olariu, C., Steel, R., Wang, H., 2020. Tectonic evolution of Tianshan-Bogda-Kelameili mountains, clastic wedge basin infill and chronostratigraphic divisions in the source-to-sink systems of Permian-Jurassic, southern Junggar Basin. Mar. Pet. Geol. 114, 104200.
Zhu, G., Yan, H., Chen, W., Yan, L., Zhang, K., Li, T., Chen, Z., et al., 2020. Discovery of Cryogenian interglacial source rocks in the northern Tarim, NW China: implications for Neoproterozoic paleoclimatic reconstructions and hydrocarbon exploration. Gondwana Res. 80, 370–384.
Zou, C.N., Dong, D.Z., Wang, S.J., Li, J.Z., Li, X.J., Wang, Y.M., Li, D.H., Cheng, K.M., 2010. Geological characteristics and resource potential of shale gas in China, petroleum exploration and development. Pet. Explor. Dev. 37 (6), 641–653.